Characterization of Gas Saturation in Tight-Sandstone Reservoirs with Rock-Physics Templates Based on Seismic *Q*

Mengqiang Pang[1]; Jing Ba[2]; and José M. Carcione[3]

Abstract: Tight-sandstone gas reservoirs have low porosity and permeability, dissimilar pore types, and generally high clay content. Partial saturation leads to local fluid flow induced by seismic waves, resulting in velocity dispersion and attenuation, and this is the reason why the dissipation factor (Q^{-1}) (inverse quality factor) is highly sensitive to fluid saturation. A relation between Q and saturation can be based on the self-consistent approximation and poroelasticity theory, to build, in principle, a two-dimensional (2D) rock-physics template. However, there is an ambiguity in the process of estimation because one value of Q may correspond to two saturations. Thus, this paper addresses this limitation. Moreover, a well-log in the Sichuan Basin and reported experimental data show that these reservoirs may have a high clay content, which affects the estimation. To take into account this factor, the hydration effect of clay is considered in the framework of the double double-porosity theory of wave propagation. Ultrasonic measurements were performed on a tight sandstone and the spectral-ratio method was used to estimate Q. Then, three-dimensional (3D) rock-physics templates are built by introducing the phase velocity ratio (V_P/V_S), clay content, and seismic Q estimated with an improved frequency-shift method. The template is calibrated and tested with ultrasonic, well-log, and seismic data and applied to estimate reservoir porosity, clay content, and gas saturation on 2D and 3D seismic data. **DOI: 10.1061/(ASCE)EY.1943-7897.0000761.**

Author keywords: Attenuation; Gas saturation; Clay content; Three-dimensional (3D) rock-physics template; Tight-sandstone reservoirs.

Introduction

With the increasing demand for hydrocarbon resources and the depletion of conventional oil and gas formations, the development of unconventional reservoirs has become essential (e.g., Liu et al. 2019; Guo et al. 2020a). Tight-sandstone gas plays an important role in global unconventional resources (Zhu et al. 2008; Khlaifat et al. 2011), with 25% of total gas production and 39% of total reserves (Zhou et al. 2019), which is one of the most important targets for exploration in China. Very recently, many works have regarded the detection of fluid in this type of reservoirs (Guo et al. 2020b; Wang et al. 2020a, b).

It is well-known that pore fluids affect the physical properties of rocks and their seismic responses (Batzle and Wang 1992). Sensitivity analysis of rock-physics properties is often used to detect reservoir fluids (Zeng et al. 2017). Experimental and theoretical studies have shown that seismic attenuation greatly depends on fluid type and saturation (Murphy 1982; Norris 1993; Amalokwu et al. 2014; Solazzi et al. 2019; Zhang et al. 2015; Ba et al. 2019). As an important indicator, wave attenuation has a more sensitive response to fluids than wave velocity (Pang et al. 2019; Müller and Gurevich 2004).

Local fluid flow induced by seismic waves is considered as the main cause of velocity dispersion and attenuation in rocks (Winker 1985; Carcione et al. 2003; White 1975; Spencer and Shine 2016; Guo and Gurevich 2020a, b). Heterogeneities that induce local flow and attenuation have been widely discussed in several works (Ren et al. 2020; Müller et al. 2010; Guo et al. 2018), such as (1) pore fluid squirted from soft to stiff pores, and (2) dissimilar medium properties, such as patchy saturation, multi mineral composition, and porosity variations. For instance, Pride et al. (2004) and Ba et al. (2011) proposed a double-porosity model by considering local fluid flow between two pore systems with different compressibility. Ba et al. (2017) combined patchy saturation and fabric (texture) in the same poroelasticity theory and proposed a double double-porosity model (DDP).

Seismic attenuation has already been used as a hydrocarbon indicator. Dasgupta and Clark (1998) analyzed field data and showed that rock lithology can be discriminated with seismic Q. Cao et al. (2018), based on geological and log data of carbonate reservoirs, combined forward modeling and seismic inversion to estimate fluid type and saturation from attenuation. Picotti et al. (2018) built a rock-physics model for patchy saturation and used Q to quantitatively relate seismic attributes with porosity, permeability and fluid saturation.

However, there is an ambiguity in the process of estimation because in gas-water reservoirs, Q^{-1} first increases and then decreases with fluid saturation, and one value of Q may correspond to two saturations (Norris 1993; Li et al. 2020; Yin et al. 1992). Thus, it is necessary to address this limitation. Many experimental studies on fluid-bearing sandstones showed that there is a monotonous correlation between the phase velocity ratio and fluid saturation (Wang 2016; Amalokwu et al. 2016), where this ratio is the P-wave velocity divided by the S-wave velocity, hereafter referred

[1]Ph.D. Candidate, School of Earth Sciences and Engineering, Hohai Univ., Nanjing 211100, China. Email: pmq@hhu.edu.cn

[2]Professor, School of Earth Sciences and Engineering, Hohai Univ., Nanjing 211100, China (corresponding author). Email: jba@hhu.edu.cn

[3]Researcher, School of Earth Sciences and Engineering, Hohai Univ., Nanjing 211100, China; Researcher, Dept. of Geophysics, National Institute of Oceanography and Applied Geophysics, Trieste 34010, Italy. Email: jose.carcione@gmail.com

Note. This manuscript was submitted on November 2, 2020; approved on January 26, 2021; published online on April 8, 2021. Discussion period open until September 8, 2021; separate discussions must be submitted for individual papers. This paper is part of the ***Journal of Energy Engineering***, © ASCE, ISSN 0733-9402.

as V_P/V_S. Zhou et al. (2019) analyzed the relation between elastic attributes and reservoir properties, for instance, fluid type, saturation and porosity, and suggested that V_P/V_S is closely related to fluid content.

The well-log data in the work area (Sichuan Basin) show that the gas reservoirs have a high clay content, which is positively correlated with fluid saturation and V_P/V_S based on the data and previous experimental studies (Han et al. 1986; Wang et al. 2006). Hence, attenuation, V_P/V_S, and impedance, based on the self-consistent approximation model and the DDP equation, are used to build a three-dimensional (3D) rock-physics template (RPT). Ultrasonic, log, and seismic data are used to calibrate the template, respectively, and apply it to two-dimensional (2D) and 3D seismic data containing three gas wells. The predictions are then compared with actual production reports.

Attenuation and Fluid Saturation: Experiment and Theory

Laboratory Measurements

To analyze the effects of fluid saturation on attenuation, ultrasonic measurements were performed on a tight sandstone sample, which has a porosity of 8.64%, a permeability of 0.00038 μm^2, and a dry-rock density of 2.41 g/cm^3. The sample is a cylinder with a length of 42.4 mm and diameter of 25.2 mm. An aluminum block with the same shape and size is processed as a reference material. The temperature is 20°C, the pore pressure is 10 MPa, and the confining pressure is 80 MPa. The wave velocities are measured with the ultrasonic-pulse method at a frequency of approximately 1 MHz, and the experimental setup (Guo et al. 2009; Ba et al. 2019) used is shown in Fig. 1.

For the partial saturation (gas-water) experiment, the full water sample is placed in an oven to change the saturation and measure the weight of the sample to calculate it. Then, the sample is sealed with a rubber sleeve, and corresponding confining and pore pressures are applied. Waveforms are recorded to obtain the velocities at different fluid saturations on the basis of the first arrivals.

Attenuation Estimation

The ultrasonic Q is estimated by using the spectral ratio method, and a standard aluminum rod with high Q is used as a reference material (Toksöz et al. 1979), such that

$$\ln\left[\frac{A_1(f)}{A_2(f)}\right] = -\frac{\pi x}{QV} f + \ln\left[\frac{G_1(f)}{G_2(f)}\right] \quad (1)$$

where V = wave velocity of the rock sample; x = distance of wave propagation; $G_1(f) - G_2(f)$ and $A_1(f) - A_2(f)$ = geometric factors and amplitude spectra of the sample and reference medium, respectively; and f = frequency. Fig. 2 shows the estimation process. The waveforms of the reference material and sample with different fluid saturations are given and several periods are selected as time windows [Fig. 2(a)]. A Fourier transform is applied to obtain the spectrum at full water saturation [Fig. 2(b)], calculate the spectrum ratio curve, perform a linear fit in the main frequency band [Fig. 2(c)], and obtain the quality factor.

Laboratory measurements to analyze the relation between the dissipation factor and gas saturation of sandstones have been performed at various frequencies, specifically 56 Hz (Li et al. 2019), 571–647 Hz (Murphy 1982), 700 Hz (Yin et al. 1992), 0.65 MHz [artificial sample (Amalokwu et al. 2014)], and 1 MHz (Wang 2016). These experimental results and those of the present study are shown in Fig. 3(a). On the other hand, Fig. 3(b) exhibits theoretical results obtained by Norris (1993) and Amalokwu et al. (2014) based on the White model (White 1975), by Müller and Gurevich (2004) based on the Johnson model for random and periodic structures (Johnson 2011), by Zhang et al. (2015) considering the variations of the correlation length in random patchy saturation, and by Solazzi et al. (2019) by using a numerical upscaling procedure (Rubino et al. 2009). The porosity of the data and models is given in the figure, and these plots indicate that attenuation increases first and then decreases with fluid saturation, and that its value is higher at full water saturation.

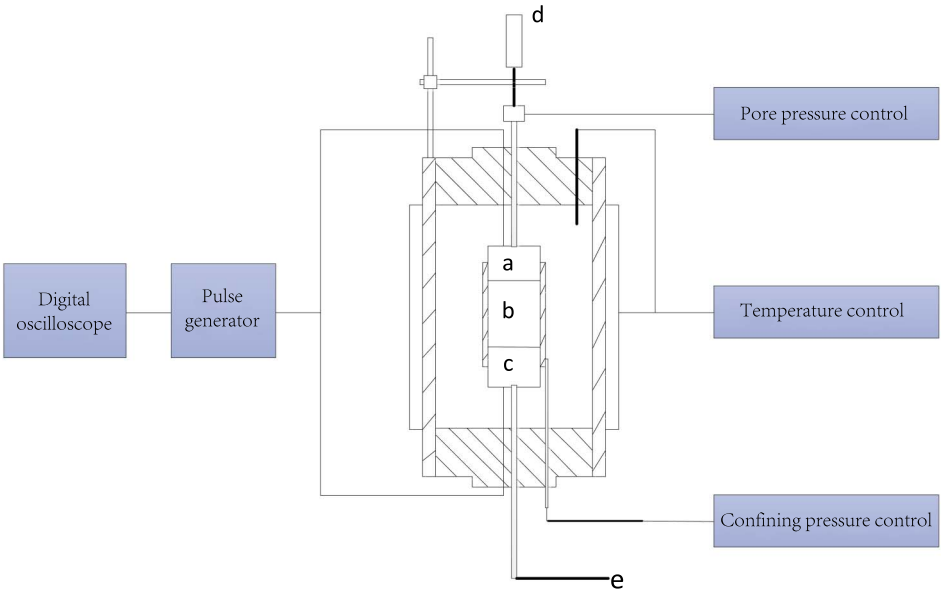

Fig. 1. Schematic of the experimental apparatus: (a) transmitting piezoelectric transducer; (b) jacketed rock sample; (c) receiving piezoelectric transducer; (d) pore fluid inlet; and (e) pore fluid outlet.

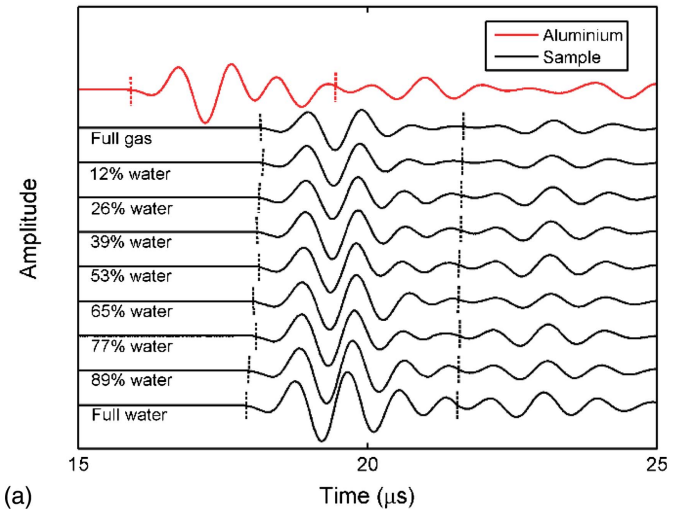

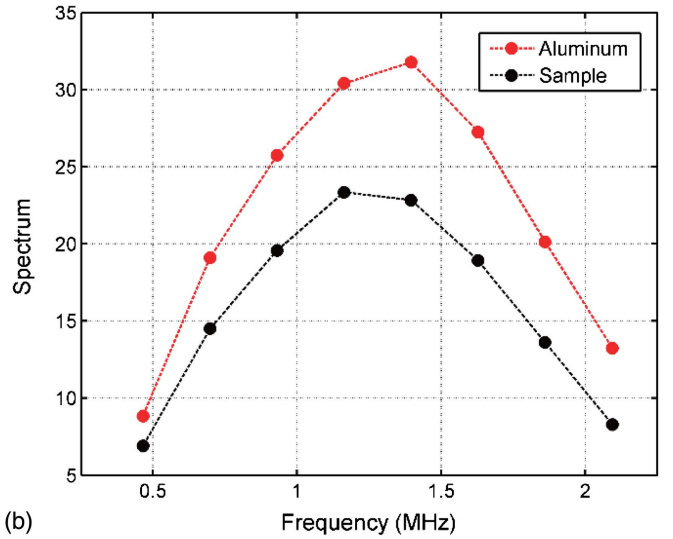

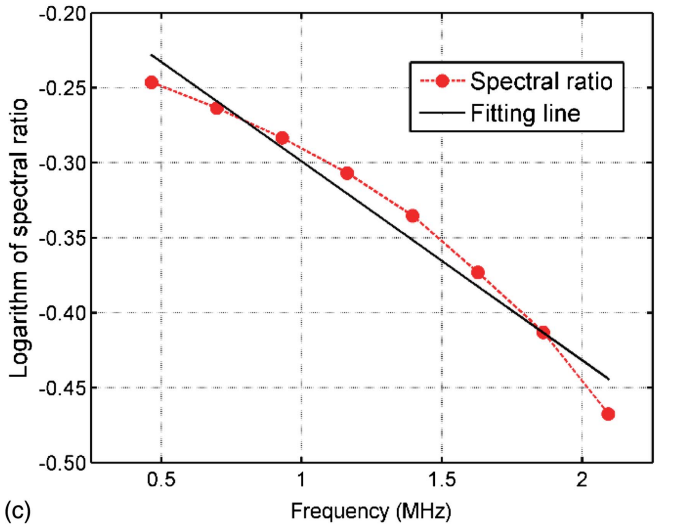

Fig. 2. Spectral-ratio method to estimate the attenuation: (a) waveforms, where the dotted line is the selected time window; (b) time spectra; and (c) spectral ratio at the main frequency band and fit.

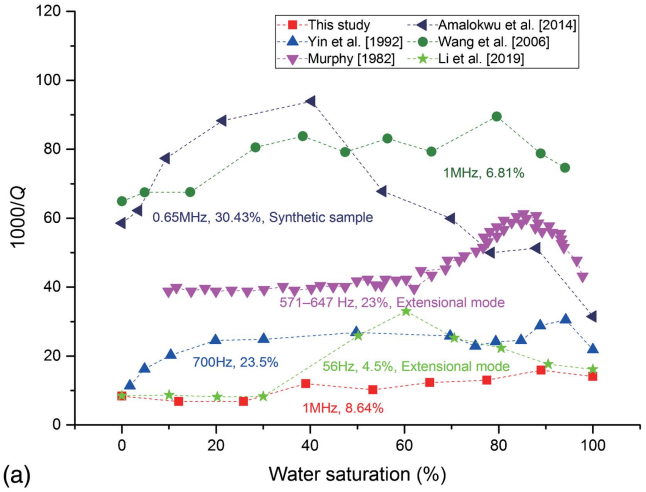

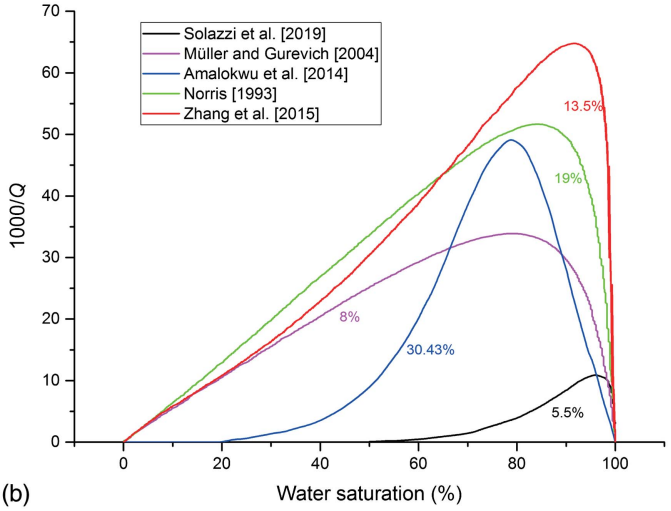

Fig. 3. Dissipation factor and water saturation, and the porosity is given: (a) measurements of this study and reported experimental results; and (b) reported theoretical models.

Rock-Physics Model

Modeling Steps

To describe the effects of rock fabric and fluid heterogeneities on seismic waves, a rock-physics model is built. First, the mineral composition is analyzed, and the elastic moduli and density of the matrix (frame) are calculated. The sandstone sample is mainly composed of quartz and clay, with a small amount of feldspar and cuttings. The bulk modulus of quartz is 37 GPa, and its shear modulus is 44 GPa; the clay bulk modulus is 25 GPa, and its shear modulus is 9 GPa; and the feldspar bulk modulus is 75.6 GPa, and its shear modulus is 25.6 GPa (Mavko et al. 2009). The Hashin-Shtrikman (HS) equations (Hashin and Shtrikman 1963) are used to obtain the bulk and shear moduli of the mineral mixture

$$K^{\mathrm{HS}\pm} = K_1 + \frac{f_2}{(K_2 - K_1)^{-1} + f_1\left(K_1 + \frac{4}{3}\mu_1\right)} \tag{2a}$$

$$\mu^{\mathrm{HS}\pm} = \mu_1 + \frac{f_2}{(\mu_2 - \mu_1)^{-1} + 2f_1(K_1 + 2\mu_1)/[5\mu(K_1 + \frac{4}{3}\mu_1)]} \tag{2b}$$

where K_1 and K_2 = bulk moduli of the individual phases; μ_1 and μ_2 = corresponding shear moduli; and f_1 and f_2 = volume fractions.

Secondly, the self-consistent approximation model (SCA) is used to add spherical pores and oblate cracks, whose aspect ratio are 1 and 0.0005, respectively, to the mineral mixture and obtain the dry-rock moduli. Berryman (1980) proposed the SCA equations to compute the composite dry-rock bulk (M^*_{SC}) and shear (G^*_{SC}) moduli

$$\sum c_i(M_i - M^*_{SC})Q^{*i} = 0 \tag{3a}$$

$$\sum c_i(G_i - G^*_{SC})P^{*i} = 0 \tag{3b}$$

where P^{*i} and Q^{*i} (Berryman 1980, p. 3) = geometrical factors of the ith component; M_i and G_i = bulk and shear moduli, respectively; and c_i = corresponding volume fractions.

Then, the Batzle and Wang (1992) equation is used to calculate the density and bulk modulus of the fluids at in situ conditions. Finally, the Biot-Rayleigh (BR) theory (Ba et al. 2011, 2012; Sun et al. 2015) is used to estimate the wave response of the saturated rock by assuming patchy gas pockets as inclusions. Based on the Hamilton principle, the local fluid flow mechanism interaction between different pore regions is substituted into strain and kinetic energy, the corresponding potential, kinetic, and dissipation functions are established, and the wave propagation equations of the double-porosity medium is obtained

$$N\nabla^2\mathbf{w} + (A+N)\nabla\varepsilon + Q_1\nabla(\xi^{(2)} + \phi_1\zeta) + Q_2\nabla(\xi^{(2)} - \phi_1\zeta) = \rho_{11}\ddot{\mathbf{w}} + \rho_{12}\ddot{\mathbf{W}}^{(1)} + \rho_{13}\ddot{\mathbf{W}}^{(2)} + b_1(\dot{\mathbf{w}} - \dot{\mathbf{W}}^{(1)}) + b_2(\dot{\mathbf{w}} - \dot{\mathbf{W}}^{(2)}) \tag{4a}$$

$$Q_1\nabla\varepsilon + R_1\nabla(\xi^{(1)} + \phi_2\zeta) = \rho_{12}\ddot{\mathbf{w}} + \rho_{22}\ddot{\mathbf{W}}^{(1)} - b_1(\dot{\mathbf{w}} - \dot{\mathbf{W}}^{(1)}) \tag{4b}$$

$$Q_2\nabla\varepsilon + R_2\nabla(\xi^{(2)} - \phi_1\zeta) = \rho_{13}\ddot{\mathbf{w}} + \rho_{33}\ddot{\mathbf{W}}^{(2)} - b_2(\dot{\mathbf{w}} - \dot{\mathbf{W}}^{(2)}) \tag{4c}$$

$$\phi_2(Q_1\varepsilon + R_1(\xi^{(1)} + \phi_2\zeta)) - \phi_1(Q_2\varepsilon + R_2(\xi^{(2)} - \phi_1\zeta)) = \frac{1}{3}\rho_f\ddot{\xi}R_0^2\frac{\phi_1^2\phi_2\phi_{20}}{\phi_{10}} + \frac{1}{3}\frac{\eta\phi_1^2\phi_2\phi_{20}}{\kappa_1}\dot{\zeta}R_0^2 \tag{4d}$$

where, $\mathbf{w}$, $\mathbf{W}^{(1)}$, and $\mathbf{W}^{(2)}$ denote the displacement vectors of the frame, host fluid, and inclusion fluid, respectively; ε, $\xi^{(1)}$, and $\xi^{(2)}$ = corresponding divergences; b_1 and b_2 = Biot's dissipation coefficients; ρ_{11}, ρ_{12}, ρ_{13}, ρ_{22}, and ρ_{33} = density coefficients; scalar ζ = fluid variation in the local fluid flow; v_1 and v_2 = volume ratios of the host medium and inclusions, respectively; ϕ_{10} and ϕ_{20} = corresponding porosities; ϕ_1 and ϕ_2 = corresponding absolute porosities ($\phi_1 = v_1\phi_{10}$ and $\phi_2 = v_2\phi_{20}$); ρ_f = fluid density; η = viscosity; κ_1 = permeability of the host medium; A, N, R_1, R_2, Q_1, and Q_2 = stiffness coefficients; and R_0 = inclusion radius.

A plane-wave analysis is performed to obtain the complex wave number k, and then the wave velocity and attenuation (Appendix).

Wave Response and Fluid Saturation

Based on the established model, the P-wave velocity dispersion and attenuation characteristics of the sandstone with different saturations are analyzed. The proportions of quartz, clay, feldspar, and cuttings are 68.4%, 15.2%, 7.6%, and 8.8%, respectively; the porosity is 8%, the permeability is 0.0015 μm^2, and the gas-patch radius is 50 μm. The fluid density, bulk modulus, and viscosity are 0.089 g/cm^3, 0.017 GPa, and 0.000016 Pa · s (gas), and 1.0016 g/cm^3, 2.24 GPa, and 0.00098 Pa · s (water), respectively. The elastic moduli of the composite mineral and skeleton are calculated by using the HS and SCA equations, respectively. The water saturation is set to 0%, 20%, 40%, 60%, 80%, and 100%, and the other parameters are kept constant.

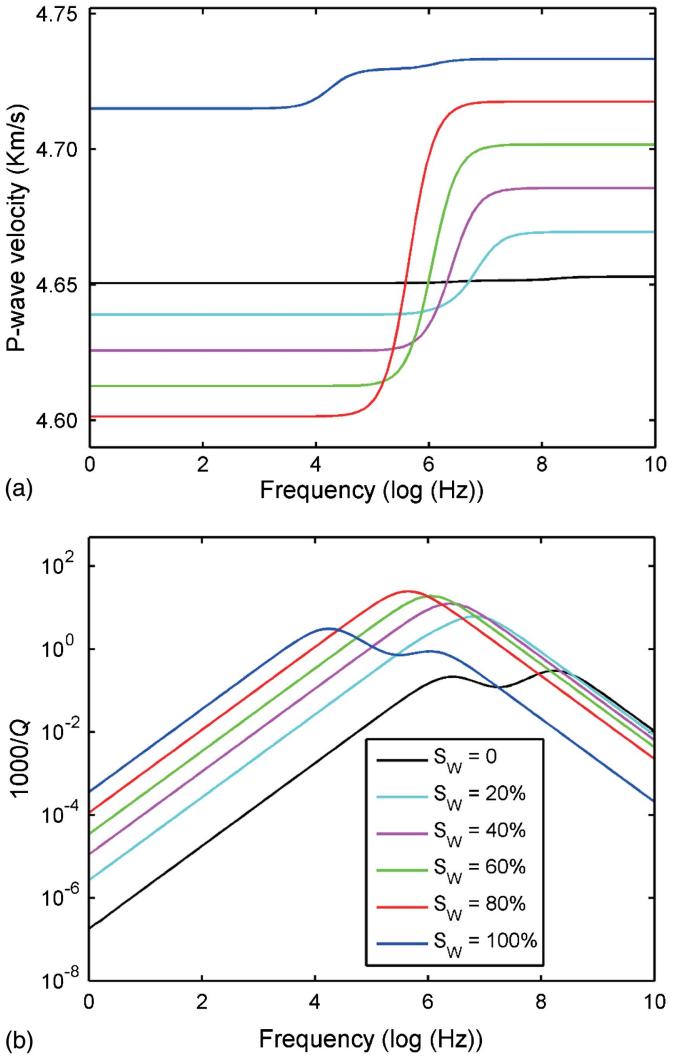

Fig. 4. (a) P-wave velocity dispersion; and (b) dissipation factor as a function of frequency for different water saturations.

Fig. 4 shows the P-wave attributes with different saturations as a function of frequency. As water saturation increases, the P-wave dissipation factor first increases and then decreases. The dispersion and corresponding attenuation peaks reach a maximum at high water saturation, which is in line with previous models and experimental results (Fig. 2).

Two-Dimensional RPT

According to the model, the attenuation and acoustical impedance (Ip) are set as the ordinate and abscissa, respectively, adjusting the water saturation and porosity to obtain a 2D template. Fig. 5 shows the RPT at 1 MHz, where the solid line corresponds to constant porosity and the other line to constant saturation. The results show that the attenuation first increases and then decreases with fluid saturation, and as porosity decreases, it shows a monotonous downward trend and the wave impedance gradually increases.

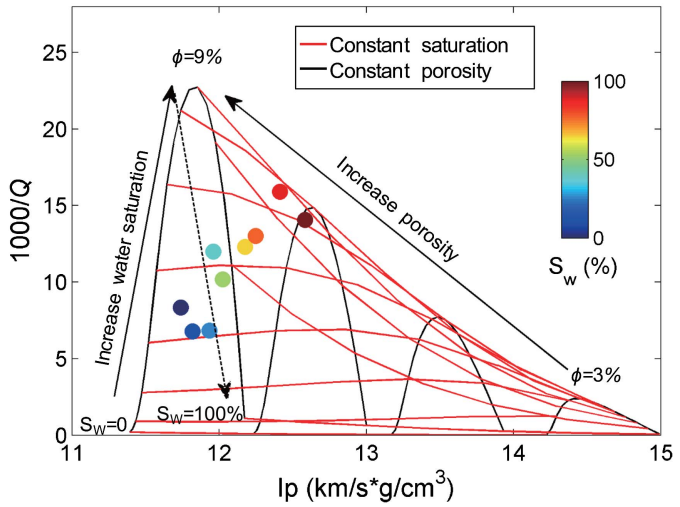

Fig. 5. Two-dimensional attenuation RPT at 1 MHz and ultrasonic sample.

The laboratory data (symbols) of this study are used to calibrate the template. By comparing the symbols with the curves, the measured porosity is in good agreement with the template. The measured saturation is basically in line with the template, and at full water saturation, the experimental attenuation is higher than that of the template. With increasing water saturation, the 2D template provides two solutions, and this is a limitation. Thus, it is necessary to improve the template to solve this problem.

Reformulated Rock-Physics Model and 3D RPT

Experimental and Well-Log Data Analysis

On the basis of published experimental data and the authors' measurements, the results show that V_P/V_S is closely related to saturation, as shown in Fig. 6(a). V_P/V_S monotonously increases with water saturation. The log data of a gas-bearing Well A in the study area is given (Fig. 7). Fig. 7(a) shows that the trend between V_P/V_S and fluid saturation is similar to that of experimental measurements.

Figs. 7(b and c) show that the clay content of the target layer is high, which is estimated from the Gamma-ray log [Eq. (10), Li 2018], and that V_P/V_S and water saturation increase with clay content. Moreover, this is also observed in the published experimental data in Fig. 6(b), where V_P/V_S varies slightly with the clay content in dry conditions, but in the water-saturated state, there is an evident monotonously increasing trend. This is due to the hydration of clay, which has a layered structure in which adsorbed water results in strong repulsive force that causes the clay to expand to several times its original thickness (Karaborni et al. 1996; Li et al. 2020). This complex physicochemical process requires energy consumption, which reduces the surface energy of clay mineral, thus reducing the contact stiffness of rock grains, softening the shear modulus of rocks (Murphy et al. 1984, 1986; Khazanehdari and Sothcott 2003; Li et al. 2020), and increasing V_P/V_S [Figs. 6(b) and 7(b)].

From Figs. 6(c) and 7(d), the porosity generally decreases gradually with clay content, the minerals filling the pores and cracks. Fig. 7(e) shows that the P- and S-wave velocities decrease with porosity, where the P-wave velocity and porosity have a linear relationship. On the other hand, Fig. 7(f) indicates that V_P/V_S decreases slightly with increasing porosity.

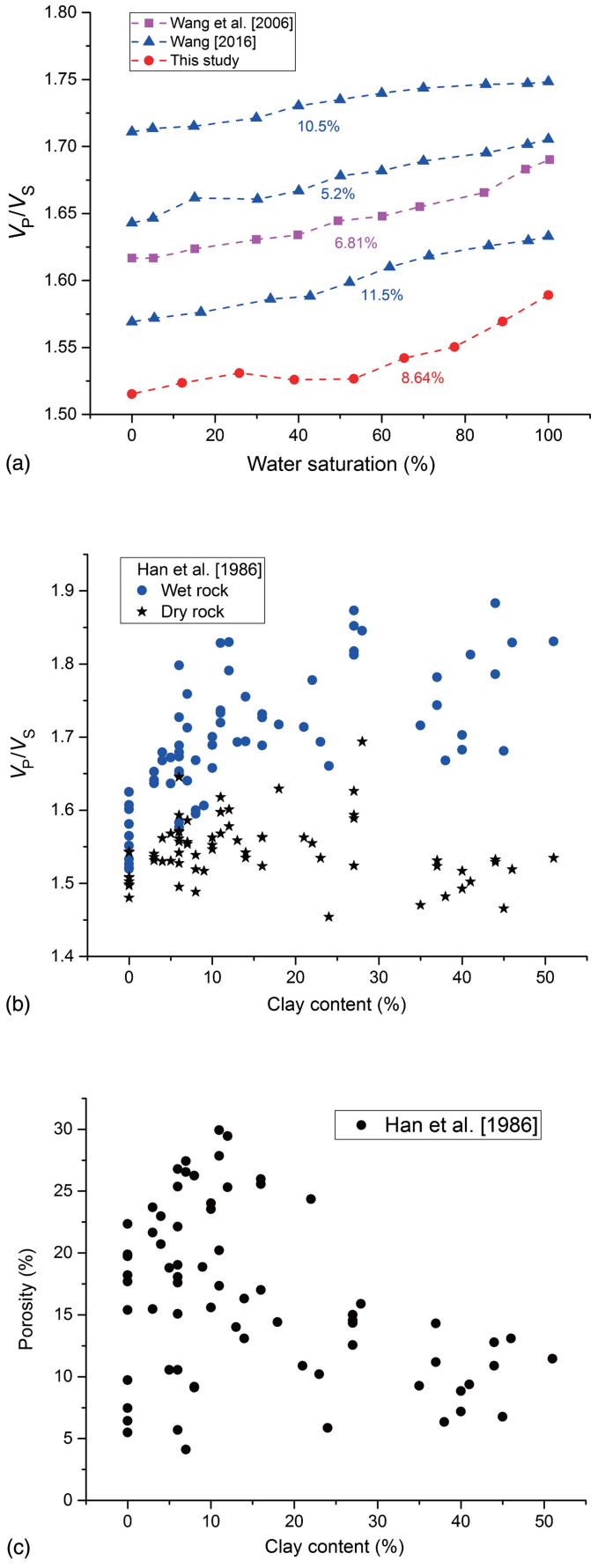

Fig. 6. Reported experiment results and our measurements: (a and b) V_P/V_S as a function of water saturation and clay content; and (c) relation between porosity and clay content.

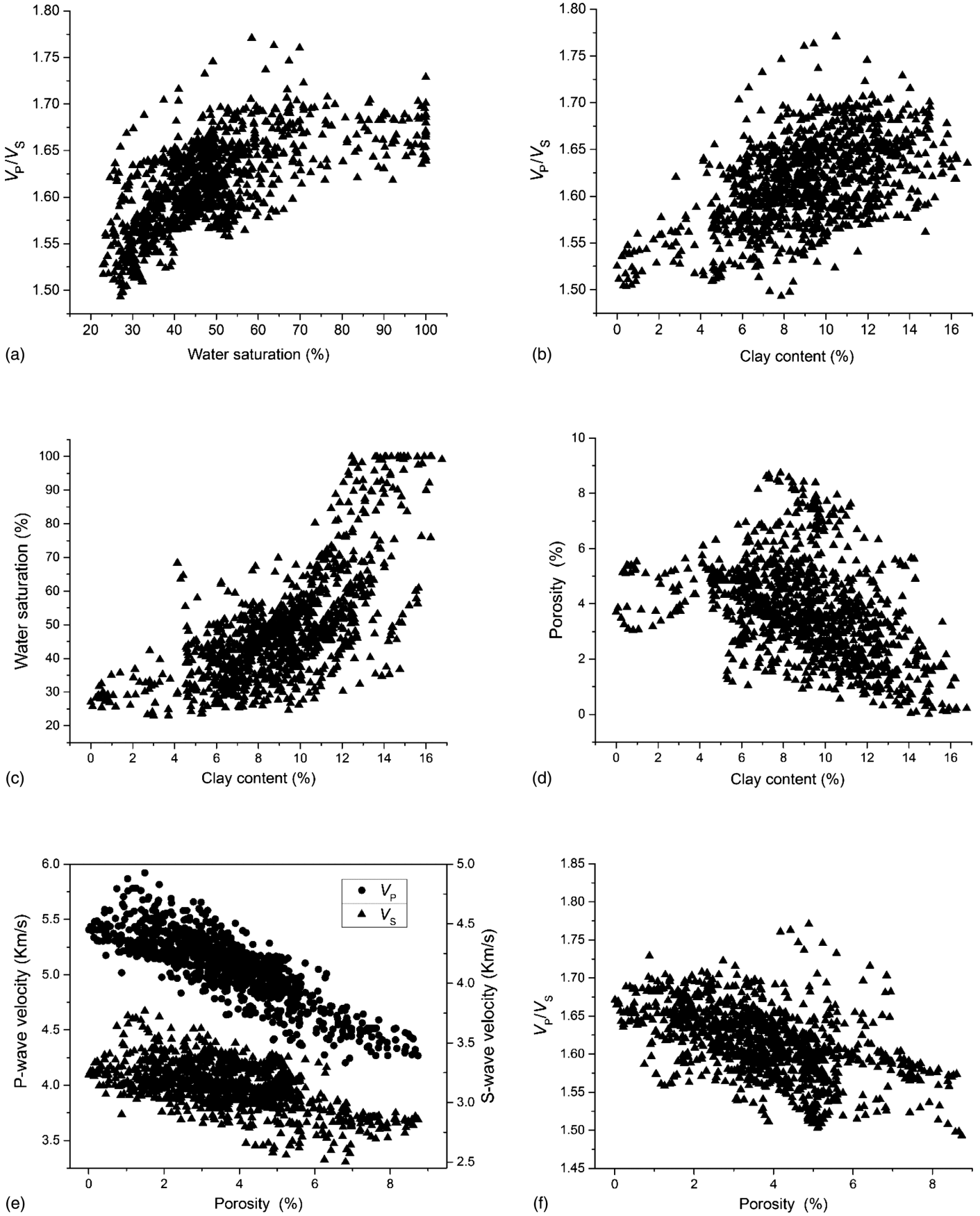

Fig. 7. Log data of Well A in the work area: (a and b) V_P/V_S as a function of water saturation and clay content; (c and d) water saturation as a function of porosity and clay content; and (e and f) P- and S-wave velocities and V_P/V_S as a function of porosity.

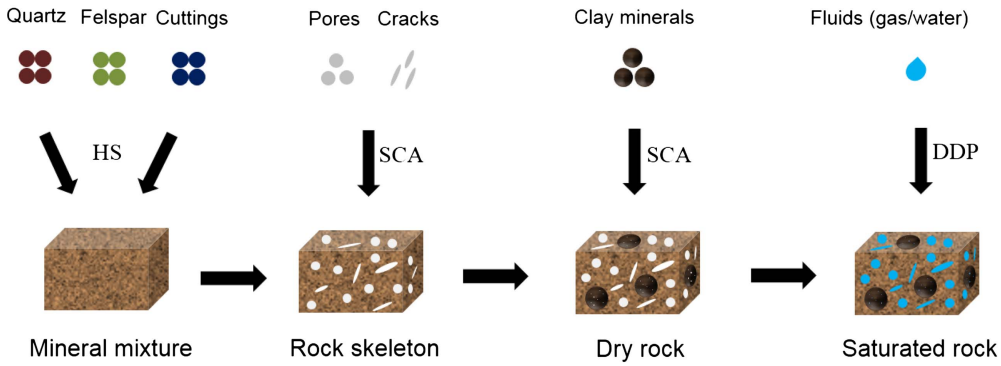

Fig. 8. Remodeling flowchart.

Model Rebuilding and Analysis

From well-log data and published experimental studies, the target layer has a relatively high clay content, which has important effects on fluid saturation and porosity. The expansions of clay with water saturation affect the particle contacts in weakly cemented sandstone, and then the elastic moduli and reservoir physical properties (Han et al. 1986; Li et al. 2020). Thus, one has to consider this effect. Ba et al. (2017) and Ma et al. (2019) regarded clay minerals in the pores as inclusions and obtained the wave properties of tight rocks by using the poroelasticity models, including velocity dispersion. Moreover, recent studies showed that there is a clay squirt-flow mechanism in argillaceous rocks, which has been successfully explained by several models (Ba et al. 2016, 2017; Marketos and Best 2010). To address the limitation of the 2D RPT and consider the effects of the clay minerals, the rock-physics model is improved as shown in Fig. 8. The clay minerals are inclusions in the DDP theory.

After adding pores and cracks to the matrix, clay minerals with micropores are added to the dry rock as inclusions to obtain the corresponding bulk and shear moduli. Thus, the double-porosity structure of the matrix and inclusions and the fluids constitute a double double-porosity model. Then, by considering patchy saturation and fabric heterogeneity, the DDP theory is used to obtain a saturated rock-physics model. Based on the Hamilton principle, the wave-propagation equations of the double double-porosity medium with the two heterogeneities are obtained (Ba et al. 2017)

$$N\nabla^2\mathbf{w} + (N+A)\nabla e + Q_1\nabla(\xi^{(1)} + \zeta_{12}\phi_2 + \zeta_{13}\phi_3) + Q_2\nabla(\xi^{(2)} - \zeta_{12}\phi_1 + \zeta_{24}\phi_4) + Q_3\nabla(\xi^{(3)} - \phi_1\zeta_{13}) + Q_4\nabla(\xi^{(4)} - \phi_2\zeta_{24})$$
$$= \rho_{00}\ddot{\mathbf{w}} + \rho_{01}\ddot{\mathbf{W}}^{(1)} + \rho_{02}\ddot{\mathbf{W}}^{(2)} + \rho_{03}\ddot{\mathbf{W}}^{(3)} + \rho_{04}\ddot{\mathbf{W}}^{(4)} + b_1(\dot{\mathbf{w}} - \dot{\mathbf{W}}^{(1)}) + b_2(\dot{\mathbf{w}} - \dot{\mathbf{W}}^{(2)}) + b_3(\dot{\mathbf{w}} - \dot{\mathbf{W}}^{(3)}) + b_4(\dot{\mathbf{w}} - \dot{\mathbf{W}}^{(4)}) \quad (5a)$$

$$Q_1\nabla e + R_1\nabla(\xi^{(1)} + \phi_2\zeta_{12} + \phi_3\zeta_{13}) = \rho_{01}\ddot{\mathbf{w}} + \rho_{11}\ddot{\mathbf{W}}^{(1)} - b_1(\dot{\mathbf{w}} - \dot{\mathbf{W}}^{(1)}) \quad (5b)$$

$$Q_2\nabla e + R_2\nabla(\xi^{(2)} - \phi_1\zeta_{12} + \phi_4\zeta_{24}) = \rho_{02}\ddot{\mathbf{w}} + \rho_{22}\ddot{\mathbf{W}}^{(2)} - b_2(\dot{\mathbf{w}} - \dot{\mathbf{W}}^{(2)}) \quad (5c)$$

$$Q_3\nabla e + R_3\nabla(\xi^{(3)} - \phi_1\zeta_{13}) = \rho_{03}\ddot{\mathbf{w}} + \rho_{33}\ddot{\mathbf{W}}^{(3)} - b_3(\dot{\mathbf{w}} - \dot{\mathbf{W}}^{(3)}) \quad (5d)$$

$$Q_4\nabla e + R_4\nabla(\xi^{(4)} - \phi_2\zeta_{24}) = \rho_{04}\ddot{\mathbf{w}} + \rho_{44}\ddot{\mathbf{W}}^{(4)} - b_4(\dot{\mathbf{w}} - \dot{\mathbf{W}}^{(4)}) \quad (5e)$$

$$\phi_2(Q_1e + R_1(\xi^{(1)} + \phi_2\zeta_{12} + \phi_3\zeta_{13})) - \phi_1(Q_2e + R_2(\xi^{(2)} - \phi_1\zeta_{12} + \phi_4\zeta_{24})) = \frac{1}{3}\rho_f^{(1)}\ddot{\zeta}_{12}R_{12}^2\frac{\phi_1^2\phi_2^2\phi_{20}}{\phi_{10}(\phi_2+\phi_4)} + \frac{1}{3}\dot{\zeta}_{12}R_{12}^2\frac{\eta_f^{(1)}\phi_1^2\phi_2^2\phi_{20}}{\kappa_1(\phi_2+\phi_4)} \quad (5f)$$

$$\phi_3(Q_1e + R_1(\xi^{(1)} + \phi_2\zeta_{12} + \phi_3\zeta_{13})) - \phi_1(Q_3e + R_3(\xi^{(2)} - \phi_1\zeta_{13})) = \frac{1}{3}\rho_f^{(1)}\ddot{\zeta}_{13}R_{13}^2\phi_1^2\phi_3 + \frac{1}{3}\dot{\zeta}_{13}R_{13}^2\frac{\eta_f^{(1)}\phi_1^2\phi_3\phi_{10}}{\kappa_1} \quad (5g)$$

$$\phi_4(Q_2e + R_2(\xi^{(2)} - \phi_1\zeta_{12} + \phi_4\zeta_{24})) - \phi_2(Q_4e + R_4(\xi^{(4)} - \phi_2\zeta_{24})) = \frac{1}{3}\rho_f^{(1)}\ddot{\zeta}_{24}R_{24}^2\phi_2^2\phi_4 + \frac{1}{3}\dot{\zeta}_{24}R_{24}^2\frac{\eta_f^{(1)}\phi_2^2\phi_4\phi_{20}}{\kappa_2} \quad (5h)$$

where, $\mathbf{w}$, $\mathbf{W}^{(1)}$, $\mathbf{W}^{(2)}$, $\mathbf{W}^{(3)}$, and $\mathbf{W}^{(4)}$ represent the displacement vectors of the frame, fluid Phases 1 and 2 in the host medium, and Phases 3 and 4 in inclusions (clay), respectively; ε, $\xi^{(1)}$, $\xi^{(2)}$, $\xi^{(3)}$, and $\xi^{(4)}$ = corresponding divergences; scalars ζ_{12}, ζ_{13}, and ζ_{24} = fluid variations in of local fluid flow; ϕ_1, ϕ_2, ϕ_3, and ϕ_4 = porosities of the four fluid phases; R_{12} = inclusion radius; R_{13} and R_{24} = gas pocket radius in host and inclusions, respectively; ϕ_{10} and ϕ_{20} = corresponding absolute porosities; v_1 and v_2 = relative volume ratios; κ_1 and κ_2 = permeabilities; $\eta_f^{(1)}$ = host fluid viscosity; $\rho_f^{(1)}$ = mass density; b_1, b_2, b_3, and b_4 = Biot's dissipation coefficients; ρ_{00}, ρ_{01}, ρ_{02}, ρ_{03}, ρ_{11}, ρ_{22}, and ρ_{33} = density coefficients; and A, N, R_1, R_2, R_3, R_4, Q_1, Q_2, Q_3, and Q_4 = stiffnesses coefficients. Velocity and attenuation can be obtained with a plane-wave analysis (Appendix).

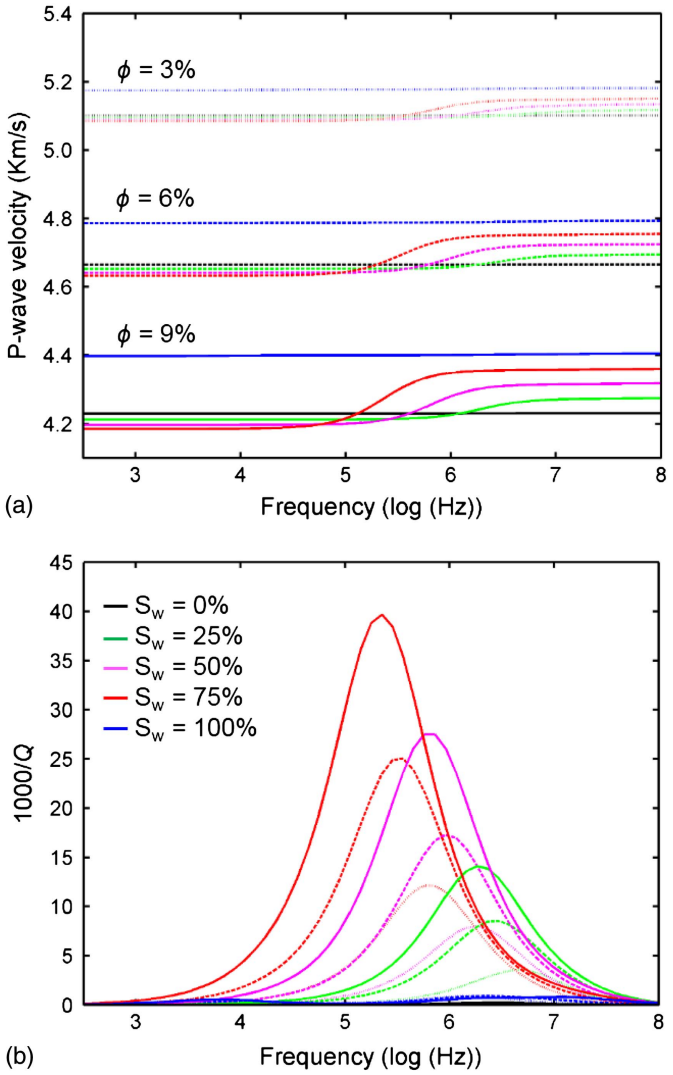

Fig. 9. (a) P-wave velocity dispersion; and (b) attenuation as a function of frequency for different water saturations and porosities.

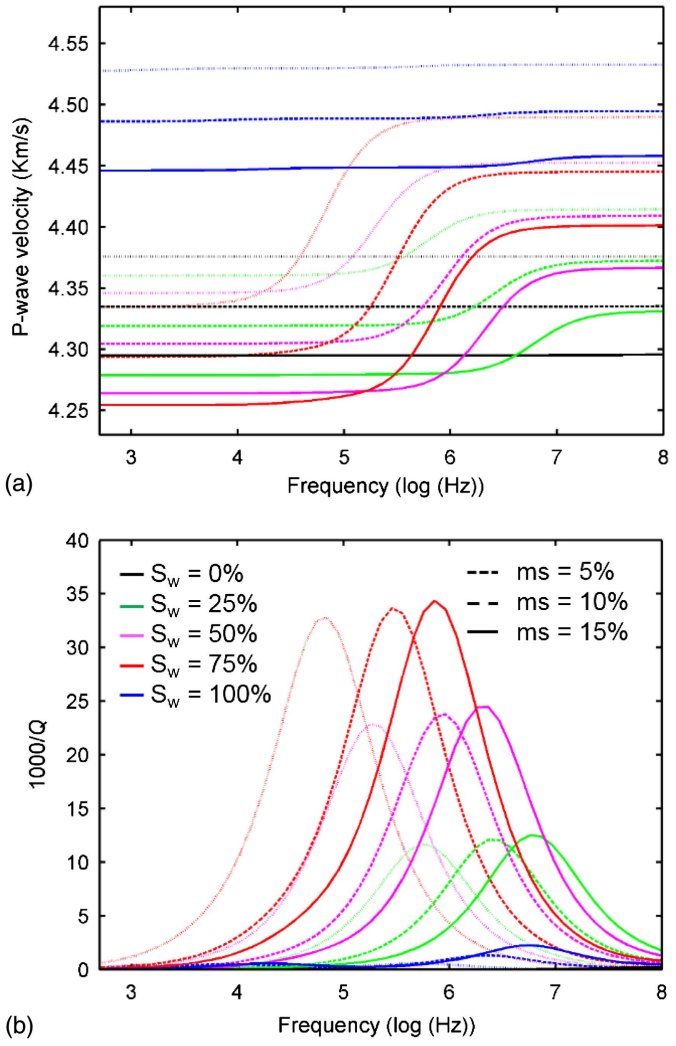

Fig. 10. (a) P-wave velocity dispersion; and (b) attenuation as a function of frequency for different water saturations and clay content.

Similarly, based on the improved model, it is analyzed how the wave response is affected by fluid saturation, clay content, and porosity. The gas-patch radii R_{13} and R_{24} are 50 and 1 μm, respectively, and the inclusion radius is 50 μm; ϕ_{20} is 0.025, and the same parameters of the 2D template are kept. The water saturation is set to 0%, 25%, 50%, 75%, and 100%, the porosity is 3%, 6%, and 9%, and the clay content is 5%, 10%, and 15%. Figs. 9 and 10 show the P-wave attributes at different saturations, porosities, and clay contents. The velocity dispersion and corresponding attenuation peaks first increase and then decrease with water saturation increase, reaching a maximum at high saturations. The figures show that the P-wave velocity decreases rapidly as porosity increases, but it slowly decreases with clay content.

Three-Dimensional RPT at Ultrasonic Frequencies

A 3D RPT at 1 MHz is given in Fig. 11 based on V_P/V_S, attenuation, and impedance. This template overcomes the ambiguity of estimating saturation with attenuation. The symbols represent the measurement, the measurement bar is water saturation, the dotted line is 2% clay content, the solid line is 12% clay content, and the black dotted line is constant porosity. Similar to the 2D template, as water saturation increases, attenuation first increases

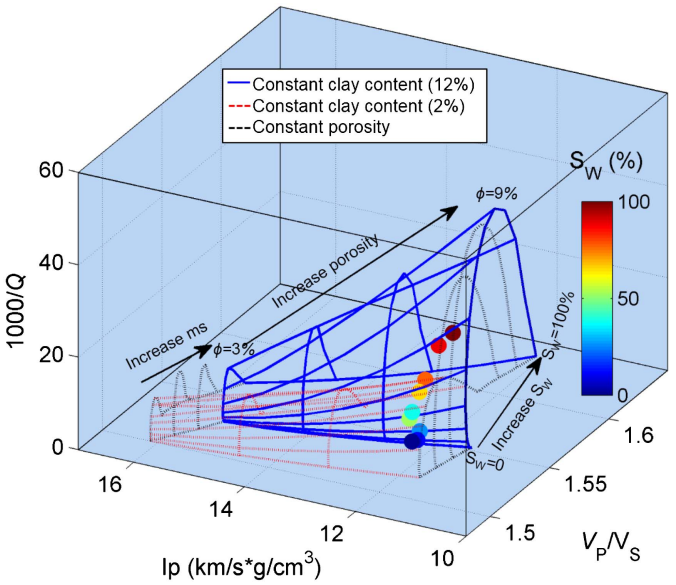

Fig. 11. Three-dimensional attenuation RPT at 1 MHz and experimental data.

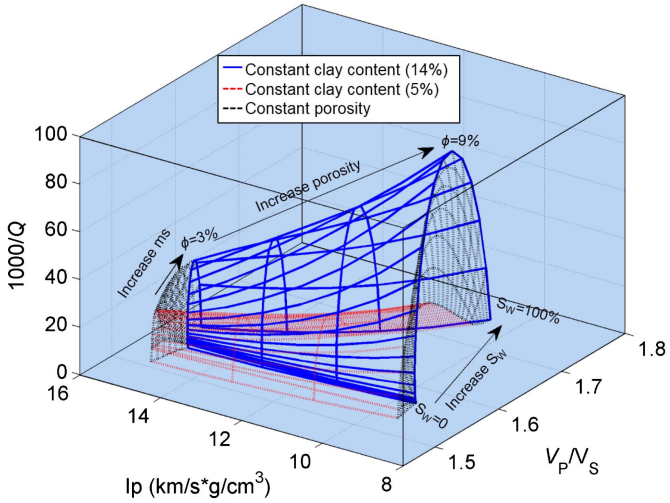

Fig. 12. Three-dimensional attenuation RPT at 35 Hz.

and then decreases, and impedance and V_P/V_S increase. As clay content increases, the fabric heterogeneity and squirt-flow effect increase, resulting in stronger attenuation. The template predicts similar wave responses of the measurement with increasing water saturation, and the porosity also agrees.

Three-Dimensional RPT at Seismic Frequencies

The rock-physics model is extended from the microscale to the mesoscale (by considering gas pockets and clay inclusions with a radius of 50 mm). Fig. 12 shows the 3D RPT at seismic frequencies (35 Hz), indicating that the wave response to fluid saturation, porosity, and clay content is similar to that of the ultrasonic template, except there is stronger attenuation in the seismic case. The 3D RPT can then be used to quantitatively characterize reservoir gas saturation.

Seismic-Attenuation Estimation

The centroid frequency-shift method was proposed by Quan and Harris (1997) to estimate the seismic Q. This method is stable when the signal-to-noise ratio is low. However, due to the assumption that the wavelet amplitude spectrum is Gaussian, there are limitations in actual applications. Zhang and Ulrych (2002) proposed a peak frequency-shift method based on the assumption that the seismic source is a Ricker wavelet, which is more reliable. However, the stability depends on the accurate extraction of the peak frequency, which is highly affected by the time window choice, noise interference, and other factors. To solve these problems, Pang et al. (2019, 2020) used an improved frequency-shift method to calculate Q by assuming a Ricker wavelet

$$Q = \frac{\sqrt{\pi^5} t f_{C1} f_{C0}^2}{16(f_{C0}^2 - f_{C1}^2)} \tag{6}$$

where f_{C0} and f_{C1} = centroid frequency of the signal before and after propagation, respectively; and t = travel time.

Based on seismic data in the study area, the generalized S-transform is used for time-frequency analysis, and Eq. (6) is used to estimate the seismic Q. Fig. 13 shows a survey line along three gas-bearing Wells, A, B, and C, where the dotted lines show their locations. The corresponding seismic amplitude and Q value profiles (Fig. 13) are given.

Seismic-Template Calibration

The 3D RPT is calibrated based on log and poststack seismic data. Attenuation is estimated by using Eq. (6), and V_P and V_P/V_S are extracted from the seismic traces around the borehole location by using a three-term inversion method (Aki and Richards 1980). Based on the prestack angle gathers, the partial stack method is used to obtain seismic data, which improves the signal-to-noise ratio and suppresses random noises, and then the more reliable inversion results are obtained. Fig. 14 shows the V_P/V_S and acoustic impedance profiles. Then, the three seismic attributes of the trace at Well A are extracted, and the log data (porosity, fluid saturation

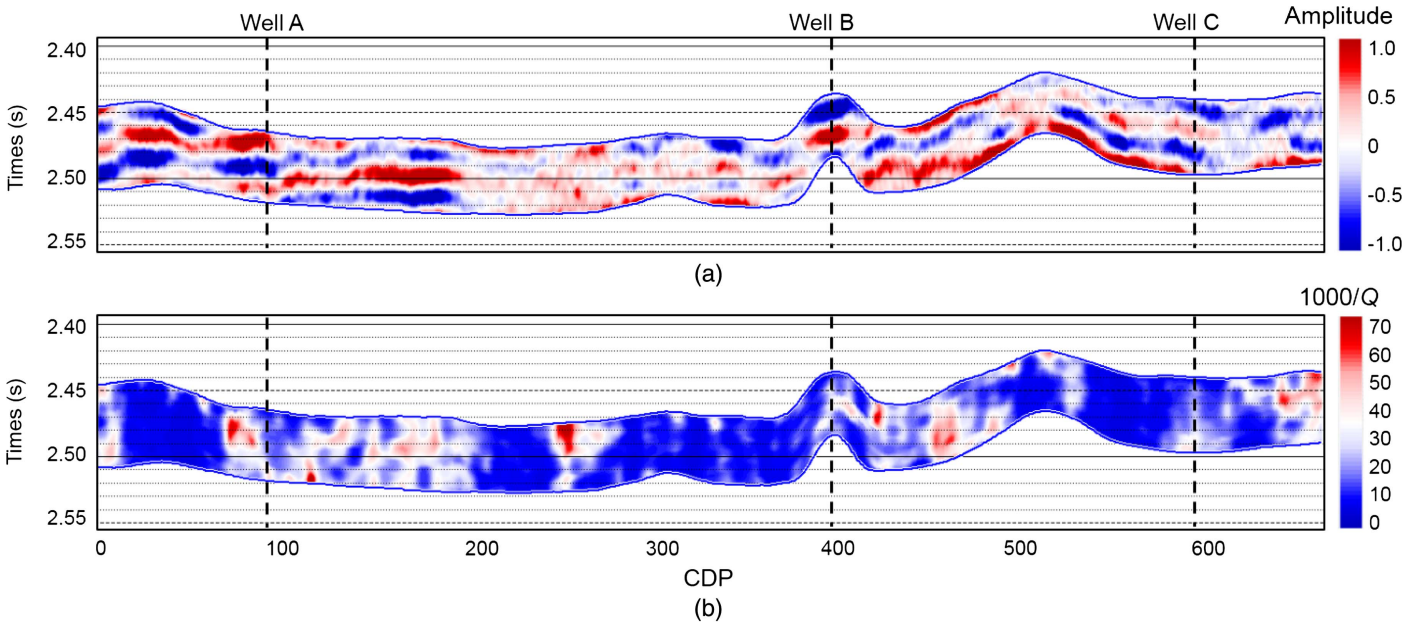

Fig. 13. Two-dimensional seismic profiles of (a) amplitude; and (b) attenuation of the target layer.

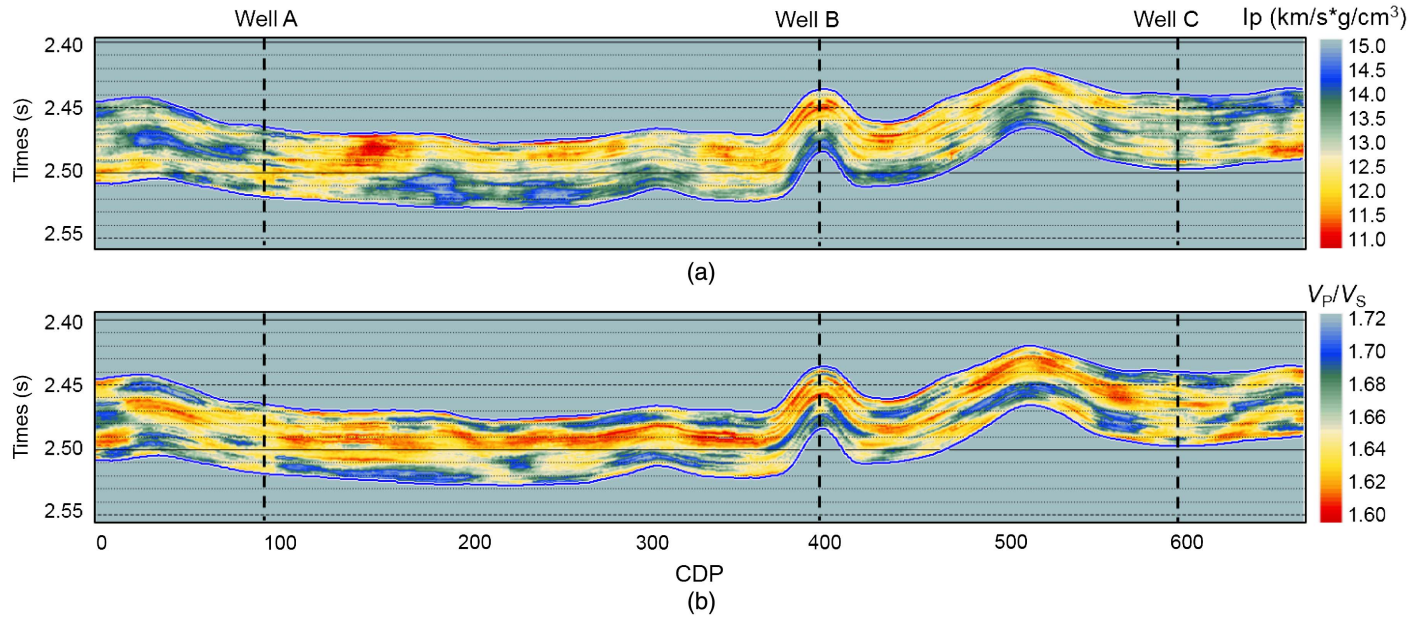

Fig. 14. Two-dimensional seismic profiles of (a) impedance; and (b) V_P/V_S of the target layer.

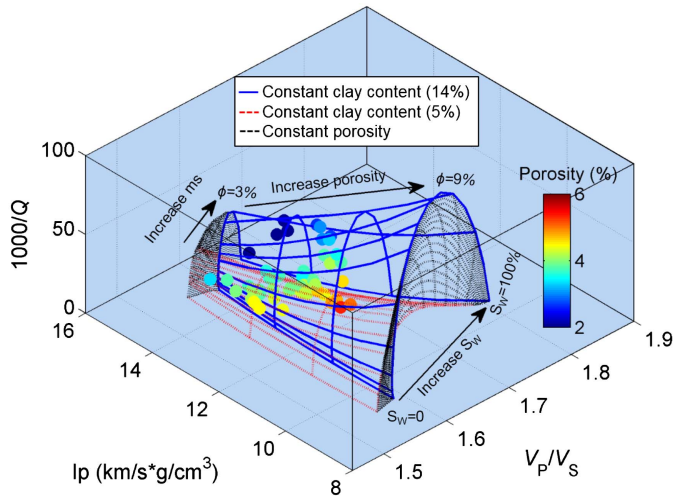

Fig. 15. Three-dimensional RPT at 35 Hz and field data. Color bar indicates porosity.

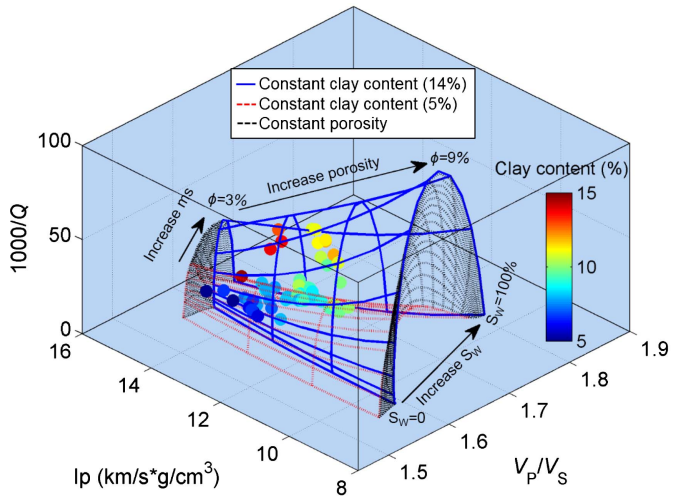

Fig. 16. Three-dimensional RPT at 35 Hz and field data. Color bar indicates clay content.

and clay content) are used as properties corresponding to the seismic data.

The seismic data are projected to calibrate the RPT, as shown in Figs. 15–17, where the measurement bars indicate porosity, clay content, and water saturation, respectively. By comparing the symbols with the RPT, the trend is consistent with the reservoir properties. The porosity is low, and the clay minerals have a good hydrophilicity. Then, a quantitative prediction of porosity, clay content, and saturation based on the RPT is performed.

Application to Seismic Data

The work area is located in the western depression belt in the Sichuan Basin, China. The tight sandstone reservoirs in this area are rich in natural gas resources, and the main gas production layer is the Xujiahe Formation of Upper Triassic. The stratum can be divided into Xu 1, 2, 3, 4, 5, and 6 sections, where Xu 2 is a lacustrine-type braided river delta sedimentary system (Wang et al. 2020c; Wu et al. 2020; Zhang et al. 2020). There are high-quality source rocks with strong hydrocarbon generation capacity and rich natural gas resources (Zhu et al. 2008).

The reservoirs are generally tight, with low porosity and permeability, forming geological features of diverse micropore structures, development of clay minerals, and heterogeneous distribution of pore fluids. The size of mineral grains is mainly medium to fine, the sorting is good, and the grains are medium-poorly rounded (Zhu et al. 2008; Wang et al. 2011). The mineral composition of the target rocks is mainly quartz, clay mineral, and a small amount of feldspar and cuttings. The depth of the target layer is about 4,700–5,200 m, the temperature is 80°C–100°C, the confining pressure range is 90–110 MPa, and pore pressure is 50–60 MPa.

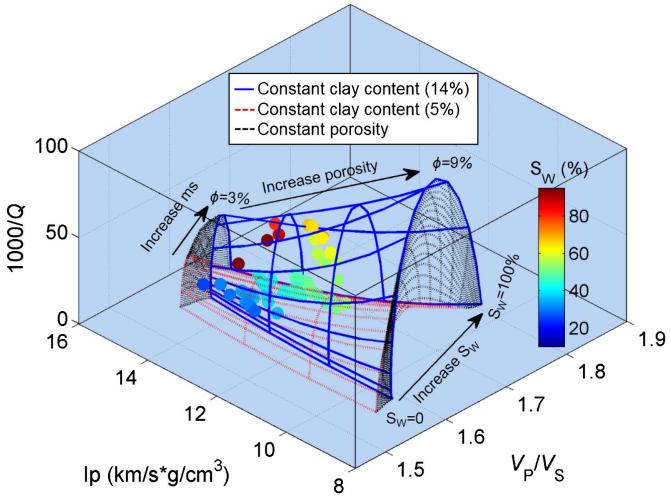

Fig. 17. Three-dimensional RPT at 35 Hz and field data. Color bar indicates water saturation.

Based on the 3D RPT, the seismic attributes are superimposed on the template, and the grid searching method is used to estimate the corresponding reservoir properties. Given the seismic data, the reservoir parameters can be estimated by minimizing the square of the difference between the seismic data and template of the three attributes. Fig. 18 shows 2D profiles of porosity, clay content, and fluid saturation, showing that porosity is about 2%–8%, and the formation is generally tight, which is consistent with the regional geology. The areas where the three wells are located all show higher porosity, where Well B has the highest gas saturation, followed by Wells C and A. The prediction of clay content is opposite to the gas saturation. By comparing the two profiles, there is a good correlation between water saturation and clay content and the areas with higher gas saturation have lower clay content.

Fig. 19 shows a 3D estimation horizontal section of porosity, clay content, and fluid saturation (92.93 km^2). The results show similar predictions as given previously. In actual gas tests, Well B is a high-production gas well, with a gas production of 1.012×10^6 m^3 per day and a water production of 9.5 m^3 per day. Well C produces 2.99819×10^5 m^3 per day of gas and 114.1 m^3 per day of water. Well A produces 3.6×10^3 m^3 per day of gas and 282 m^3 per day of water. Comparing the actual production reports and estimations, the predictions are consistent.

Conclusions

This study has developed a methodology to predict gas saturation, porosity, and clay content in tight sandstones by using rock-physics templates based on seismic Q. First, ultrasonic experiments were performed and Q was calculated with a spectral-ratio method. These measurements and previous experimental and theoretical studies show and confirm that attenuation is very sensitive to fluid saturation. Then, the authors established a rock-physics model by using the self-consistent approximation and a double-porosity

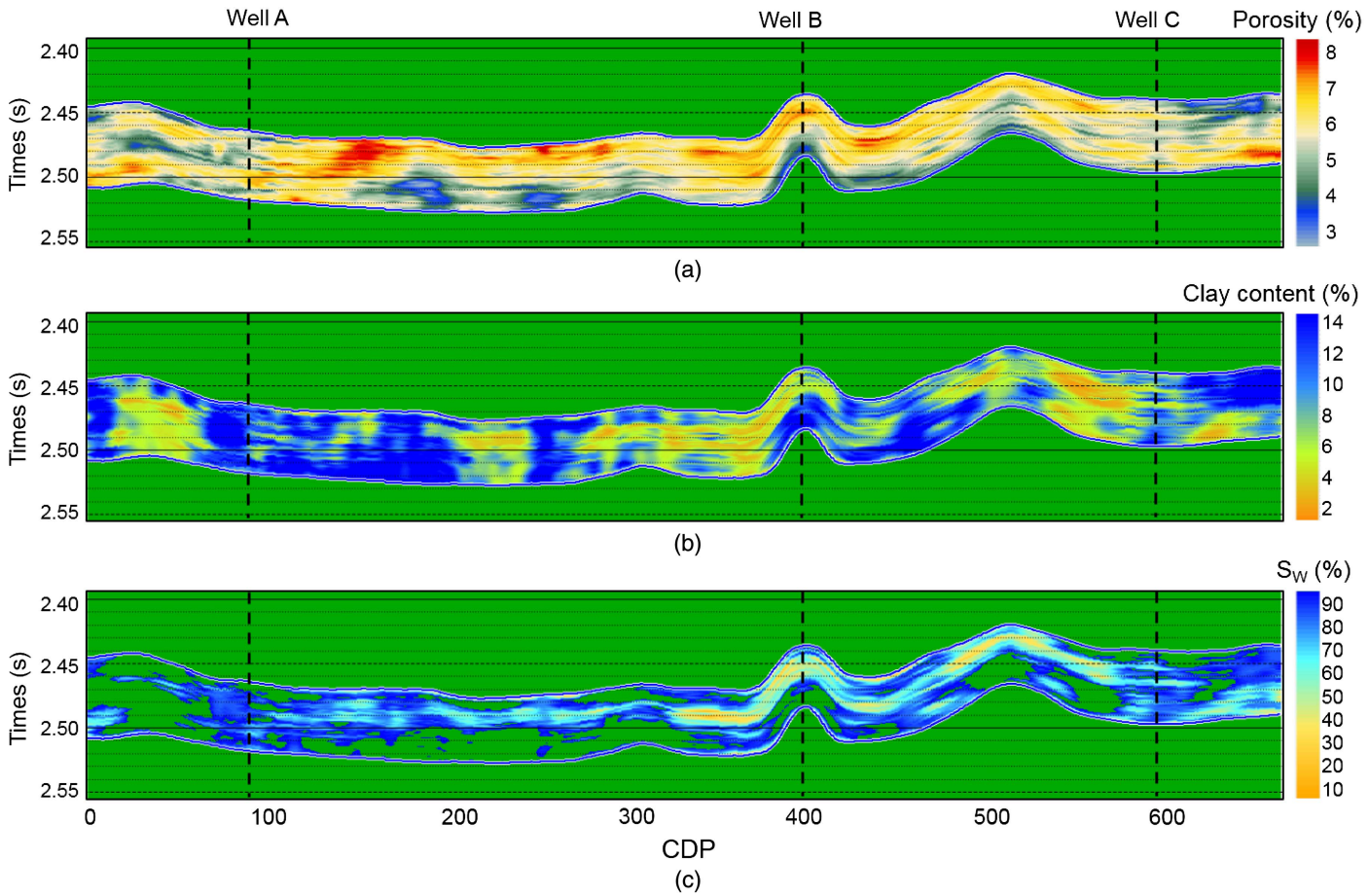

Fig. 18. Two-dimensional estimation results of (a) porosity; (b) clay content; and (c) water saturation.

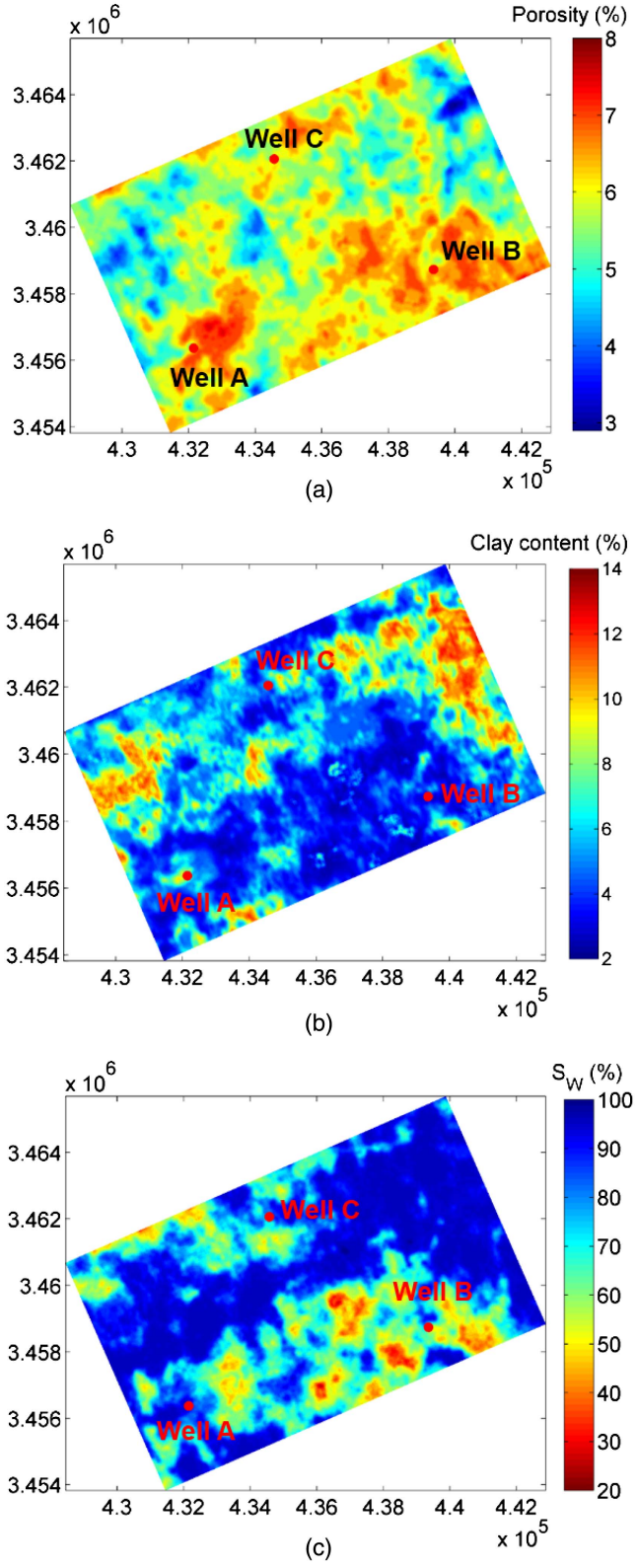

Fig. 19. Three-dimensional horizontal section estimation results of (a) porosity; (b) clay content; and (c) water saturation.

theory to obtain the wave response. Based on these models, a 2D RPT was built by using Q and calibrated with ultrasonic data.

The template is able to distinguish fluid saturation, but there is an ambiguity that limits its application because the same Q can be related to different saturations. Moreover, the effect of hydration of clay must be considered because it affects saturation and V_P/V_S. Hence, clay minerals are considered as inclusions, and the model was improved by using a double double-porosity theory to model the effects of fluid and fabric heterogeneities. This leads to a 3D RPT, which overcomes the ambiguity and takes into account the hydration of clays. By using an improved frequency-shift method to obtain Q, the template was calibrated with the ultrasonic, well-log, and seismic data, respectively. The method was applied to 2D and 3D seismic data, showing that the estimations are consistent with gas production reports at three wells in the Sichuan Basin.

Appendix. Dispersion Equations and Clay-Volume Estimation

Dispersion Equation of the BR Theory

Substituting a plane P-wave kernel into Eqs. (4*a*)–(4*d*) yields the complex wave number k

$$\begin{vmatrix} a_{11}k^2+b_{11} & a_{12}k^2+b_{12} & a_{13}k^2+b_{13} \\ a_{21}k^2+b_{21} & a_{22}k^2+b_{22} & a_{23}k^2+b_{23} \\ a_{31}k^2+b_{31} & a_{32}k^2+b_{32} & a_{33}k^2+b_{33} \end{vmatrix} = 0 \tag{7a}$$

where

$$\begin{aligned} &a_{11}=A+2N+\mathrm{i}(Q_2\phi_1-Q_1\phi_2)x_1,\\ &b_{11}=-\rho_{11}\omega^2+\mathrm{i}\omega(b_1+b_2)\\ &a_{12}=Q_1+\mathrm{i}(Q_2\phi_1-Q_1\phi_2)x_2,\quad b_{12}=-\rho_{12}\omega^2-\mathrm{i}\omega b_1\\ &a_{13}=Q_2+\mathrm{i}(Q_2\phi_1-Q_1\phi_2)x_3,\quad b_{13}=-\rho_{13}\omega^2-\mathrm{i}\omega b_2\\ &a_{21}=Q_1-\mathrm{i}R_1\phi_2x_3,\quad b_{21}=-\rho_{12}\omega^2-\mathrm{i}\omega b_1\\ &a_{22}=R_1-\mathrm{i}R_1\phi_2x_2,\quad b_{22}=-\rho_{22}\omega^2+\mathrm{i}\omega b_1\\ &a_{23}=-\mathrm{i}R_1\phi_2x_3,\quad b_{23}=0,\quad a_{31}=Q_2+\mathrm{i}R_2\phi_1x_1,\\ &b_{31}=-\rho_{13}\omega^2-\mathrm{i}\omega b_2,\quad a_{32}=\mathrm{i}R_2\phi_1x_2,\\ &b_{32}=0a_{33}=R_2+\mathrm{i}R_2\phi_1x_3,\quad b_{33}=-\rho_{33}\omega^2+\mathrm{i}\omega b_2 \end{aligned} \tag{7b}$$

and

$$\begin{aligned} &x_1=\mathrm{i}(\phi_2Q_1-\phi_1Q_2)/Z,\qquad x_2=\mathrm{i}\phi_2R_1/Z,\\ &x_3=-\mathrm{i}\phi_1R_2/Z\\ &Z=\frac{\mathrm{i}\omega\eta\phi_1^2\phi_2\phi_{20}R_0^2}{3\kappa_{10}}-\frac{\rho_f\omega^2R_0^2\phi_1^2\phi_2\phi_{20}}{3\phi_{10}}-(\phi_2^2R_1+\phi_1^2R_2) \end{aligned} \tag{7c}$$

The P-wave velocity and quality factor can be expressed in terms of the complex velocity $v=\omega/k$ (Carcione 2014)

$$V_P=[\mathrm{Re}(v^{-1})]^{-1} \tag{8a}$$

$$Q=\frac{\mathrm{Re}(v^2)}{\mathrm{Im}(v^2)} \tag{8b}$$

Dispersion Equation of the DDP Theory

Similarly, by substituting a plane-wave kernel into Eqs. (5*a*)–(5*h*), one obtains

$$\begin{vmatrix} a_{11}k^2+b_{11} & a_{12}k^2+b_{12} & a_{13}k^2+b_{13} & a_{14}k^2+b_{14} & a_{15}k^2+b_{15} \\ a_{21}k^2+b_{21} & a_{22}k^2+b_{22} & a_{23}k^2+b_{23} & a_{24}k^2+b_{24} & a_{25}k^2+b_{25} \\ a_{31}k^2+b_{31} & a_{32}k^2+b_{32} & a_{33}k^2+b_{33} & a_{34}k^2+b_{34} & a_{35}k^2+b_{35} \\ a_{41}k^2+b_{41} & a_{42}k^2+b_{42} & a_{43}k^2+b_{43} & a_{44}k^2+b_{44} & a_{45}k^2+b_{45} \\ a_{51}k^2+b_{51} & a_{52}k^2+b_{52} & a_{53}k^2+b_{53} & a_{54}k^2+b_{54} & a_{55}k^2+b_{55} \end{vmatrix} = 0 \tag{9a}$$

where

$$a_{11} = A + 2N + (Q_1\phi_2 - Q_2\phi_1)M_0^{(12)} + (Q_1\phi_3 - Q_3\phi_1)M_0^{(13)} + (Q_2\phi_4 - Q_4\phi_2)M_0^{(24)}$$
$$a_{12} = Q_1 + (Q_1\phi_2 - Q_2\phi_1)M_1^{(12)} + (Q_1\phi_3 - Q_3\phi_1)M_1^{(13)} + (Q_2\phi_4 - Q_4\phi_2)M_1^{(24)}$$
$$a_{13} = Q_2 + (Q_1\phi_2 - Q_2\phi_1)M_2^{(12)} + (Q_1\phi_3 - Q_3\phi_1)M_2^{(13)} + (Q_2\phi_4 - Q_4\phi_2)M_2^{(24)}$$
$$a_{14} = Q_3 + (Q_1\phi_2 - Q_2\phi_1)M_3^{(12)} + (Q_1\phi_3 - Q_3\phi_1)M_3^{(13)} + (Q_2\phi_4 - Q_4\phi_2)M_3^{(24)}$$
$$a_{15} = Q_4 + (Q_1\phi_2 - Q_2\phi_1)M_4^{(12)} + (Q_1\phi_3 - Q_3\phi_1)M_4^{(13)} + (Q_2\phi_4 - Q_4\phi_2)M_4^{(24)}$$
$$a_{21} = Q_1 + R_1\phi_2 M_0^{(12)} + R_1\phi_3 M_0^{(13)}, \qquad a_{22} = R_1 + R_1\phi_2 M_1^{(12)} + R_1\phi_3 M_1^{(13)}$$
$$a_{33} = R_2 - R_2\phi_1 M_2^{(12)} + R_2\phi_4 M_2^{(24)}, \qquad a_{34} = -R_2\phi_1 M_3^{(12)} + R_2\phi_4 M_3^{(24)} a_{35} = -R_2\phi_1 M_4^{(12)} + R_2\phi_4 M_4^{(24)},$$
$$a_{41} = Q_3 - R_3\phi_1 M_0^{(13)}, \qquad a_{42} = -R_3\phi_1 M_1^{(13)}, \qquad a_{43} = -R_3\phi_1 M_2^{(13)} \qquad a_{44} = R_3 - R_3\phi_1 M_3^{(13)},$$
$$a_{45} = -R_3\phi_1 M_4^{(13)} \qquad a_{51} = Q_4 - R_4\phi_2 M_0^{(24)}, \qquad a_{52} = -R_4\phi_2 M_1^{(24)}, \qquad a_{53} = -R_4\phi_2 M_2^{(24)} \qquad a_{54} = -R_4\phi_2 M_3^{(24)},$$
$$a_{55} = R_4 - R_4\phi_2 M_4^{(24)} \qquad b_{11} = -\rho_{00}\omega^2 + \mathrm{i}\omega(b_1 + b_2 + b_3 + b_4), \qquad b_{12} = -\rho_{01}\omega^2 - \mathrm{i}\omega b_1,$$
$$b_{13} = -\rho_{02}\omega^2 - \mathrm{i}\omega b_2 \qquad b_{14} = -\rho_{03}\omega^2 + \mathrm{i}\omega b_3, \qquad b_{15} = -\rho_{04}\omega^2 - \mathrm{i}\omega b_4, \qquad b_{21} = -\rho_{01}\omega^2 - \mathrm{i}\omega b_1,$$
$$b_{22} = -\rho_{11}\omega^2 + \mathrm{i}\omega b_1 \qquad b_{23} = b_{24} = b_{25} = 0, \qquad b_{31} = -\rho_{02}\omega^2 - \mathrm{i}\omega b_2, \qquad b_{33} = -\rho_{22}\omega^2 + \mathrm{i}\omega b_2,$$
$$b_{32} = b_{34} = b_{35} = 0 \qquad b_{41} = -\rho_{03}\omega^2 - \mathrm{i}\omega b_3, \qquad b_{44} = -\rho_{33}\omega^2 + \mathrm{i}\omega b_3, \qquad b_{42} = b_{43} = b_{45} = 0 \qquad b_{51} = -\rho_{04}\omega^2 - \mathrm{i}\omega b_4,$$
$$b_{55} = -\rho_{44}\omega^2 + \mathrm{i}\omega b_4, \qquad b_{52} = b_{53} = b_{54} = 0 \tag{9b}$$

where

$$M_0^{(12)} = \frac{(Q_1\phi_2 - Q_2\phi_1)/S_{12} + R_1\phi_2\phi_3(Q_1\phi_3 - Q_3\phi_1)/(S_{12}S_{13}) - R_2\phi_1\phi_4(Q_2\phi_4 - Q_4\phi_2)/(S_{12}S_{24})}{1 - (R_1\phi_2\phi_3)^2/(S_{12}S_{13}) - (R_2\phi_1\phi_4)^2/(S_{12}S_{24})}$$
$$M_1^{(12)} = \frac{R_1\phi_2/S_{12} + \phi_2(R_1\phi_3)^2/(S_{12}S_{13})}{1 - (R_1\phi_2\phi_3)^2/(S_{12}S_{13}) - (R_2\phi_1\phi_4)^2/(S_{12}S_{24})}$$
$$M_2^{(12)} = \frac{-R_2\phi_1/S_{12} - \phi_1(R_2\phi_4)^2/(S_{12}S_{24})}{1 - (R_1\phi_2\phi_3)^2/(S_{12}S_{13}) - (R_2\phi_1\phi_4)^2/(S_{12}S_{24})}$$
$$M_3^{(12)} = \frac{-\phi_1\phi_2\phi_4 R_1 R_3/(S_{12}S_{13})}{1 - (R_1\phi_2\phi_3)^2/(S_{12}S_{13}) - (R_2\phi_1\phi_4)^2/(S_{12}S_{24})}$$
$$M_4^{(12)} = \frac{\phi_1\phi_2\phi_4 R_2 R_4/(S_{12}S_{24})}{1 - (R_1\phi_2\phi_3)^2/(S_{12}S_{13}) - (R_2\phi_1\phi_4)^2/(S_{12}S_{24})}$$
$$M_0^{(13)} = (M_0^{(12)}R_1\phi_2\phi_3 + \phi_3 Q_1 - \phi_1 Q_3)/S_{13}, \qquad M_1^{(13)} = (M_1^{(12)}R_1\phi_2\phi_3 + \phi_3 R_1)/S_{13}$$
$$M_2^{(13)} = (M_2^{(12)}R_1\phi_2\phi_3)/S_{13}, \qquad M_3^{(13)} = (M_3^{(12)}R_1\phi_2\phi_3 - \phi_3 R_1)/S_{13}$$
$$M_4^{(13)} = (M_4^{(12)}R_1\phi_2\phi_3)/S_{13}, \qquad M_0^{(24)} = (-M_0^{(12)}R_2\phi_1\phi_4 + Q_2\phi_4 - Q_4\phi_2)/S_{24}$$
$$M_1^{(24)} = (-M_1^{(12)}R_2\phi_1\phi_4)/S_{24}, \qquad M_2^{(24)} = (-M_2^{(12)}R_2\phi_1\phi_4 + R_2\phi_4)/S_{24}$$
$$M_3^{(24)} = (-M_3^{(12)}R_2\phi_1\phi_4)/S_{24}, \qquad M_4^{(24)} = (-M_4^{(12)}R_2\phi_1\phi_4 - R_2\phi_4)/S_{24}$$
$$S_{12} = \frac{\mathrm{i}\omega\eta_f^{(1)}R_{12}^2\phi_1^2\phi_2^2\phi_{20}}{3(\phi_2+\phi_4)\kappa_1} - \frac{\rho_f^{(1)}\omega^2 R_{12}^2\phi_1^2\phi_2^2\phi_{20}}{3\phi_{10}(\phi_2+\phi_4)} - (\phi_2^2 R_1 + \phi_1^2 R_2)$$
$$S_{13} = \frac{\mathrm{i}\omega\eta_f^{(1)}R_{13}^2\phi_1^2\phi_3\phi_{10}}{3\kappa_1} - \frac{\rho_f^{(1)}\omega^2 R_{13}^2\phi_1^2\phi_3}{3} - (\phi_3^2 R_1 + \phi_1^2 R_3)$$
$$S_{24} = \frac{\mathrm{i}\omega\eta_f^{(1)}R_{24}^2\phi_2^2\phi_4\phi_{20}}{3\kappa_2} - \frac{\rho_f^{(1)}\omega^2 R_{24}^2\phi_2^2\phi_4}{3} - (\phi_4^2 R_2 + \phi_2^2 R_4) \tag{9c}$$

The P-wave velocity and quality factor can be obtained from the complex wave number k, as in the BR theory.

Clay-Volume Estimation

The gamma ray (Gr) log yields the clay content. The equations are (Li 2018)

$$I_{Gr} = (Gr - Gr_{\min})/(Gr_{\max} - Gr_{\min}) \quad (10a)$$

$$Ms = (2^{\beta * I_{Gr}} - 1)/(2^{\beta} - 1) \quad (10b)$$

where I_{GR} = mud-content index; Gr, $Gr_{\min}$, and $Gr_{\max}$ = natural gamma values of the layer, sandstone, and mudstone, respectively; Ms = clay volume; and β = Hirsch index (3.7).

Data Availability Statement

All data, models, or code that support the findings of this study are available from the corresponding author upon reasonable request.

Acknowledgments

This work is supported by the National Natural Science Foundation of China (Grant No. 41974123), the research funds from SINOPEC Key Laboratory of Geophysics, the Jiangsu Innovation and Entrepreneurship Plan and the Jiangsu Province Science Fund for Distinguished Young Scholars (Grant No. BK20200021).

References

Aki, K., and P. G. Richards. 1980. *Quantitative seismology: Theory and methods*. San Francisco: W.H. Freeman and Company.

Amalokwu, K., I. A. Best, J. Sothcott, and M. Chapman. 2016. "Effects of aligned fractures on the response of velocity and attenuation ratios to water saturation variation: A laboratory study using synthetic sandstones." *Geophys. Prospect.* 64 (4): 942–957. https://doi.org/10.1111/1365-2478.12378.

Amalokwu, K., I. A. Best, J. Sothcott, M. Chapman, T. Minshull, and Y. Li. 2014. "Water saturation effects on elastic wave attenuation in porous rocks with aligned fractures." *Geophys. J. Int.* 197 (2): 943–947. https://doi.org/10.1093/gji/ggu076.

Ba, J., J. M. Carcione, H. Cao, Q. Du, Z. Yuan, and M. Lu. 2012. "Velocity dispersion and attenuation of P waves in partially-saturated rocks: Wave propagation equations in double-porosity medium." *Chin. J. Geophys.* 55 (1): 219–231. https://doi.org/10.6038/j.issn.0001-5733.2012.01.021.

Ba, J., J. M. Carcione, and J. Nie. 2011. "Biot-Rayleigh theory of wave propagation in double-porosity media." *J. Geophys. Res.* 116 (6): B06202. https://doi.org/10.1029/2010JB008185.

Ba, J., R. Ma, J. M. Carcione, and S. Picotti. 2019. "Ultrasonic wave attenuation dependence on saturation in tight oil siltstones." *J. Pet. Sci. Eng.* 179 (Aug): 1114–1122. https://doi.org/10.1016/j.petrol.2019.04.099.

Ba, J., W. Xu, L. Y. Fu, J. M. Carcione, and L. Zhang. 2017. "Rock anelasticity due to patchy-saturation and fabric heterogeneity: A double-double porosity model of wave propagation." *J. Geophys. Res. Solid Earth* 122 (3): 1949–1976. https://doi.org/10.1002/2016JB013882.

Ba, J., J. Zhao, J. M. Carcione, and X. Huang. 2016. "Compressional wave dispersion due to rock matrix stiffening by clay squirt flow." *Geophys. Res. Lett.* 43 (12): 6186–6195. https://doi.org/10.1002/2016GL069312.

Batzle, M., and Z. J. Wang. 1992. "Seismic properties of pore fluids." *Geophysics* 57 (11): 1396–1408. https://doi.org/10.1190/1.1443207.

Berryman, J. G. 1980. "Long-wavelength propagation in composite elastic media." *J. Acoust. Soc. Am.* 68 (6): 1809–1831. https://doi.org/10.1121/1.385171.

Cao, Z., X. Li, J. Liu, X. Qin, S. Sun, Z. Li, and Z. Cao. 2018. "Carbonate fractured gas reservoir prediction based on P-wave azimuthal anisotropy and dispersion." *J. Geophys. Eng.* 15 (5): 2139–2149. https://doi.org/10.1088/1742-2140/aabe58.

Carcione, J. M. 2014. "Wave fields in real media." In *Theory and numerical simulation of wave propagation in anisotropic, anelastic, porous and electromagnetic media*, 3rd ed. Amsterdam, Netherlands: Elsevier.

Carcione, J. M., H. B. Helle, and N. H. Pham. 2003. "White's model for wave propagation in partially saturated rocks: Comparison with poroelastic numerical experiments." *Geophysics* 68 (4): 1389–1398. https://doi.org/10.1190/1.1598132.

Dasgupta, R., and R. A. Clark. 1998. "Estimation of Q from surface seismic reflection data." *Geophysics* 63 (6): 2120–2128. https://doi.org/10.1190/1.1444505.

Guo, J., and B. Gurevich. 2020a. "Effects of coupling between wave-induced fluid flow and elastic scattering on P-wave dispersion and attenuation in rocks with aligned fractures." *J. Geophys. Res. Solid Earth* 125 (3): e2019JB018685. https://doi.org/10.1029/2019JB018685.

Guo, J., and B. Gurevich. 2020b. "Frequency-dependent P-wave anisotropy due to wave-induced fluid flow and elastic scattering in a fluid-saturated porous medium with aligned fractures." *J. Geophys. Res. Solid Earth* 125 (8): e2020JB020320. https://doi.org/10.1029/2020JB020320.

Guo, J., M. Li, C. Chen, L. Tao, Z. Liu, and D. Zhou. 2020a. "Experimental investigation of spontaneous imbibition in tight sandstone reservoirs." *J. Pet. Sci. Eng.* 193 (Oct): 107395. https://doi.org/10.1016/j.petrol.2020.107395.

Guo, J., R. Xie, and L. Xiao. 2020b. "Pore-fluid characterizations and microscopic mechanisms of sedimentary rocks with three-dimensional NMR: Tight sandstone as an example." *J. Nat. Gas Sci. Eng.* 80 (Aug): 103392. https://doi.org/10.1016/j.jngse.2020.103392.

Guo, M., L. Fu, and J. Ba. 2009. "Comparison of stress-associated coda attenuation and intrinsic attenuation from ultrasonic measurements." *Geophys. J. Int.* 178 (1): 447–456. https://doi.org/10.1111/j.1365-246X.2009.04159.x.

Guo, M. Q., J. Ba, R. Ma, T. Chen, L. Zhang, M. Pang, and J. Xie. 2018. "P-wave velocity dispersion and attenuation in fluid-saturated tight sandstones: Characteristics analysis based on a double double-porosity structure model description." *Chin. J. Geophys.* 61 (3): 1053–1068. https://doi.org/10.6038/cjg2018L0678.

Han, D., A. Nur, and D. Morgani. 1986. "Effects of porosity and clay content on wave velocities in sandstones." *Geophysics* 51 (11): 2093–2107. https://doi.org/10.1190/1.1442062.

Hashin, Z., and S. Shtrikman. 1963. "A variational approach to the elastic behavior of multiphase materials." *J. Mech. Phys. Solids* 11 (2): 127–140. https://doi.org/10.1016/0022-5096(63)90060-7.

Johnson, D. 2001. "Theory of frequency dependent acoustics in patchy-saturated porous media." *J. Acoust. Soc. Am.* 110 (2): 682–694. https://doi.org/10.1121/1.1381021.

Karaborni, S., B. Smit, W. Heidug, and E. van Oort. 1996. "The swelling of clays: Molecular simulations of the hydration of montmorillonite." *Science* 271 (5252): 1102–1104. https://doi.org/10.1126/science.271.5252.1102.

Khazanehdari, J., and J. Sothcott. 2003. "Variation in dynamic elastic shear modulus of sandstone upon fluid saturation and substitution." *Geophysics* 68 (2): 472–481. https://doi.org/10.1190/1.1567213.

Khlaifat, A. L., H. Qutob, and N. Barakat. 2011. "Tight gas sands development is critical to future world energy resources." In *Proc., SPE Middle East Unconventional Gas Conf. and Exhibition.* Nova Scotia, Canada: Society of Petroleum Engineers. https://doi.org/10.2118/142049-MS.

Li, D., J. Wei, B. Di, D. Shuai, L. Tian, and P. Ding. 2020. "Effect of fluid saturation on the shear modulus of artificial clay-rich tight sandstones." *Geophys. J. Int.* 222 (1): 15–26. https://doi.org/10.1093/gji/ggaa124.

Li, Z. 2018. *Processing and comprehensive interpretation of geophysical well-logging data*. Beijing: Geological Publisher.

Liu, D., W. Sun, and D. Ren. 2019. "Experimental investigation of pore structure and movable fluid traits in tight sandstone." *Processes* 7 (3): 149. https://doi.org/10.3390/pr7030149.

Ma, R., J. Ba, J. M. Carcione, X. Zhou, and F. Li. 2019. "Dispersion and attenuation of compressional waves in tight oil reservoirs: Experiments and simulations." *Appl. Geophys.* 16 (1): 33–45. https://doi.org/10.1007/s11770-019-0748-3.

Marketos, G., and A. I. Best. 2010. "Application of the BISQ model to clay squirt flow in reservoir sandstones." *J. Geophys. Res.* 115 (6): B06209. https://doi.org/10.1029/2009JB006495.

Mavko, G., T. Mukerji, and J. Dvorkin. 2009. *The rock physics handbook: Tools for seismic analysis of porous media*. Cambridge, UK: Cambridge University Press.
Müller, T. M., and B. Gurevich. 2004. "One-dimensional random patchy saturation model for velocity and attenuation in porous rocks." *Geophysics* 69 (5): 1166–1172. https://doi.org/10.1190/1.1801934.
Müller, T. M., B. Gurevich, and M. Lebedev. 2010. "Seismic wave attenuation and dispersion resulting from wave-induced flow in porous rocks—A review." *Geophysics* 75 (5): 147–164. https://doi.org/10.1190/1.3463417.
Murphy, W. F. 1982. "Effects of partial water saturation on attenuation in Massilon sandstone and Vycor porous glass." *J. Acoust. Soc. Am.* 71 (6): 639–648. https://doi.org/10.1121/1.387843.
Murphy, W. F., K. W. Winkler, and R. L. Kleinberg. 1984. "Frame modulus reduction in sedimentary rocks: The effect of adsorption on grain contacts." *Geophys. Res. Lett.* 11 (9): 805–808. https://doi.org/10.1029/GL011i009p00805.
Murphy, W. F., K. W. Winkler, and R. L. Kleinberg. 1986. "Acoustic relaxation in sedimentary rocks: Dependence on grain contacts and fluid saturation." *Geophysics* 51 (3): 757–766. https://doi.org/10.1190/1.1442128.
Norris, A. N. 1993. "Low-frequency dispersion and attenuation in partially saturated rocks." *J. Acoust. Soc. Am.* 94 (1): 359–370. https://doi.org/10.1121/1.407101.
Pang, M., J. Ba, J. M. Carcione, S. Picotti, J. Zhou, and R. Jiang. 2019. "Estimation of porosity and fluid saturation in carbonates from rock-physics templates based on seismic Q." *Geophysics* 84 (6): 25–36. https://doi.org/10.1190/geo2019-0031.1.
Pang, M., J. Ba, L. Fu, J. M. Carcione, U. I. Markus, and L. Zhang. 2020. "Estimation of microfracture porosity in deep carbonate reservoirs based on 3D rock-physics templates." *Interpretation* 8 (4): 43–52. https://doi.org/10.1190/INT-2019-0258.1.
Picotti, S., J. M. Carcione, and J. Ba. 2018. "Rock-physics templates for seismic Q." *Geophysics* 84 (1): 13–23. https://doi.org/10.1190/geo2018-0017.1.
Pride, S. R., J. G. Berryman, and J. M. Harris. 2004. "Seismic attenuation due to wave induced flow." *J. Geophys. Res.* 109 (1): B01201. https://doi.org/10.1029/2003JB002639.
Quan, Y. L., and J. M. Harris. 1997. "Seismic attenuation tomography using the frequency shift method." *Geophysics* 62 (3): 895–905. https://doi.org/10.1190/1.1444197.
Ren, S., T. Han, and L. Fu. 2020. "Theoretical and experimental study of P-wave attenuation in partially saturated sandstones under different pressures." *Chin. J. Geophys.* 63 (7): 2722–2736. https://doi.org/10.6038/cjg2020O0021.
Rubino, J. G., C. L. Ravazzoli, and J. E. Santos. 2009. "Equivalent viscoelastic solids for heterogeneous fluid-saturated porous rocks." *Geophysics* 74 (1): 1–13. https://doi.org/10.1190/1.3008544.
Solazzi, S. G., L. Guarracino, J. G. Rubino, and K. Holliger. 2019. "Saturation hysteresis effects on the seismic signatures of partially saturated heterogeneous porous rocks." *J. Geophys. Res.* 124 (11): 11316–11335.
Spencer, J. M., and J. Shine. 2016. "Seismic wave attenuation and modulus dispersion in sandstone." *Geophysics* 81 (3): 211–231. https://doi.org/10.1190/geo2015-0342.1.
Sun, W., J. Ba, T. M. Müller, J. M. Carcione, and H. Cao "2015Comparison of P-wave attenuation models of wave-induced flow." *Geophys. Prospect.* 63 (2): 378–390. https://doi.org/10.1111/1365-2478.12196.
Toksöz, M. N., H. D. Johnston, and A. Timur. 1979. "Attenuation of seismic waves in dry and saturated rocks: I. Laboratory measurements." *Geophysics* 44 (4): 681–690. https://doi.org/10.1190/1.1440969.
Wang, B., X. Zhao, W. Zhou, B. Chang, and H. Xu. 2020a. "Quantitative characterization of pore connectivity and movable fluid distribution of tight sandstones: A case study of the upper Triassic Chang 7 Member, Yanchang formation in Ordos Basin, China." *Geofluids* 2020 (Jan): 23. https://doi.org/10.1155/2020/5295490.
Wang, C., S. Huang, Z. Sun, Z. Hu, K. Huang, and H. Dong. 2011. "Characteristics and origin of fractures in tight sandstone reservoirs of the Xujiahe Formation in the Western Sichuan depression: A case study in the Xiaoquan—Xinchang—Hexingchang area." *Nat. Gas Indus.* 31 (8): 43–47.
Wang, D. 2016. "Study on the rock physics model of gas reservoirs in tight sandstone." *Chin. J. Geophys.* 59 (12): 4603–4622. https://doi.org/10.6038/cjg20161222.
Wang, D., K. Xin, Y. Li, J. Gao, and X. Wu. 2006. "An experimental study of influence of water saturation on velocity and attenuation in sandstone under stratum conditions." *Chin. J. Geophys.* 49 (3): 908–914.
Wang, P., J. Li, X. Chen, and B. Wang. 2020b. "Joint probabilistic fluid discrimination of tight sandstone reservoirs based on Bayes discriminant and deterministic rock physics modeling." *J. Pet. Sci. Eng.* 191 (Aug): 107218. https://doi.org/10.1016/j.petrol.2020.107218.
Wang, Q., D. Chen, X. Gao, F. Wang, J. Li, W. Liao, Z. Wang, and G. Xie. 2020c. "Microscopic pore structures of tight sandstone reservoirs and their diagenetic controls: A case study of the Upper Triassic Xujiahe Formation of the Western Sichuan Depression, China." *Mar. Pet. Geol.* 113 (Mar):104119. https://doi.org/10.1016/j.marpetgeo.2019.104119.
White, J. E. 1975. "Computed seismic speeds and attenuation in rocks with partial gas saturation." *Geophysics* 40 (2): 224–232. https://doi.org/10.1190/1.1440520.
Winkler, K. W. 1985. "Dispersion analysis of velocity and attenuation in Berea sandstone." *J. Geophys. Res.* 90 (8): 6793–6800. https://doi.org/10.1029/JB090iB08p06793.
Wu, D., S. Liu, H. Chen, L. Lin, Y. Yu, C. Xu, and B. Pan. 2020. "Investigation and prediction of diagenetic facies using well logs in tight gas reservoirs: Evidences from the Xu-2 member in the Xinchang structural belt of the western Sichuan Basin, western China." *J. Pet. Sci. Eng.* 192 (Sep): 107326. https://doi.org/10.1016/j.petrol.2020.107326.
Yin, C., M. L. Batzle, and B. J. Smith. 1992. "Effects of partial liquid/gas saturation on extensional wave attenuation in Berea sandstone." *Geophys. Res. Lett.* 19 (13): 1399–1402. https://doi.org/10.1029/92GL01159.
Zeng, Q., M. Guo, R. Jiang, J. Ba, H. Ma, and J. Liu. 2017. "Fluid sensitivity of rock physics parameters in reservoirs: Quantitative analysis." *J. Seismic Explor.* 26 (2): 125–140.
Zhang, C., and T. J. Ulrych. 2002. "Estimation of quality factors from CMP records." *Geophysics* 67 (5): 1542–1547. https://doi.org/10.1190/1.1512799.
Zhang, J., H. Zheng, G. Wang, Z. Liu, Y. Qi, Z. Huang, and X. Fan. 2020. "In-situ stresses, abnormal pore pressures and their impacts on the Triassic Xujiahe reservoirs in tectonically active western Sichuan Basin." *Mar. Pet. Geol.* 122 (Dec): 104708. https://doi.org/10.1016/j.marpetgeo.2020.104708.
Zhang, Y., O. Nishizawa, T. Kiyama, and Z. Xue. 2015. "Saturation-path dependency of P-wave velocity and attenuation in sandstone saturated with CO2 and brine revealed by simultaneous measurements of waveforms and X-ray computed tomography images." *Geophysics* 80 (4): 403–415. https://doi.org/10.1190/GEO2014-0289.1.
Zhou, H., D. Li, X. Liu, Y. Du, and W. Gong. 2019. "Sweet spot prediction in tight sandstone reservoir based on well-bore rock physical simulation." *Pet. Sci.* 16 (6): 1285–1300. https://doi.org/10.1007/s12182-019-00393-1.
Zhu, R., C. Zou, N. Zhang, X. Wang, R. Cheng, L. Liu, C. Zhou, and L. Song. 2008. "Diagenetic fluids evolution and genetic mechanism of tight sandstone gas reservoirs in Upper Triassic Xujiahe Formation in Sichuan Basin, China." *Sci. China Ser. D Earth Sci.* 51 (9): 1340–1353. https://doi.org/10.1007/s11430-008-0102-8.